Laboratory for Aero & Hydrodynamics

Transient turbulence in Taylor Couette flow

Arjang Alidai, 4035429
Master Thesis, Mechanical engineering, SFM

Exam commission:
Prof.dr.ir. J. Westerweel, TU Delft
Dr. R. Delfos, TU Delft
Dr.ir. G.E. Elsinga, TU Delft
Dr.ir. A. Talmon, TU Delft
August 25, 2011
MEAH-259

Acknowledgements

I would like to express my special appreciation to the members of Taylor Couette team at Laboratory for Aero & Hydrodynamics in Delft University of Technology: Prof.dr.ir. J. Westerweel, Dr. R. Delfos, Dr.ir. G.E. Elsinga, Ir. A. Greidanus and Ir. S. Tokgöz. Thanks for giving me the opportunity to be part of this leading research team.

My gratitude also goes to our workshop technician, Jasper Ruijgrok, whose excellent work did make everything so much faster and easier. I would also like to appreciate all people in the Laboratory who support me throughout this research project.

The most special thanks goes to my family. You gave me your unconditional support and love all this long process. Thank you so much.

Contents

Summary

The most recent studies of intermittent state in linearly stable shear flows, like pipe, Plane Couette and Taylor Couette flow, have shown that turbulent structures, created by finite-amplitude perturbation, have an exponential distribution of the lifetimes. Here we experimentally examine the lifetime of turbulent spot in Taylor Couette flow (with stationary inner cylinder) for different perturbation mechanisms and different boundary conditions. We show that for all of these cases, the decay of the turbulent spot can be described by Poisson process, which supports the chaotic transient model for this flow. Furthermore, we show that characteristic lifetime of the turbulent spot increases with Reynolds number faster than exponentially, but does not diverge to infinity. This is in agreement with the most recent studies in pipe and Taylor Couette flows and implies that turbulence is a transient state for all Reynolds numbers (before the global bifurcation). Finally, we show that there is a universal behavior for the characteristic lifetime of the intermittent state in Taylor Couette flow with stationary inner cylinder. This universal series is obtained using critical Reynolds number and aspect ratio as scaling parameters.

List of Symbols and Abbreviations

Symbol	Description	Page
Re	Reynolds number	page 1
ν	Kinematic viscosity of fluid	page 1
τ	Characteristic lifetime	page 3
Ω_i	Angular velocity of inner cylinder	page 9
Ω_o	Angular velocity of outer cylinder	page 9
r_i	Radius of inner cylinder	page 9
r_o	Radius of outer cylinder	page 9
ρ	Density of fluid	page 11
R_i	Reynolds number of inner cylinder	page 11
R_o	Reynolds number of outer cylinder	page 11
η	Radius ratio	page 11
R_Ω	Rotation number	page 12
R_c	Curvature number	page 12
Re_{cr}	Critical Reynolds number	page 15
Γ	Aspect ratio	page 16
I_{avg}	Average image matrix of laminar flow	page 19
I	Image matrix	page 19
N	Standard deviation of normalized light intensity	page 19
α	Threshold for separating laminar from turbulent region in image	page 21
Re_h	Reynolds number bases on Von Kármán gap	page 24
f_{cyl}	Frequency of outer cylinder	page 44
f_{patch}	Rotational frequency of patch	page 43
U_{patch}	Traveling speed of patch	page 43
f_{cam}	Camera frequency	page 60

Abbreviation	Description	Page
2-d	Two dimensional	page 8
CFD	Computational Fluid Dynamic	page 22
PIV	Particle Image Velocimetry	page 22
LDV	Laser Doppler Velocimetry	page 22
FVM	Finite Volume Method	page 28
MUSCL	Monotone Upstream-centered Schemes for Conservation Laws	page 28

List of Figures

Chapter 1

Introduction

1.1 Transition to turbulence

In supercritical flows (where laminar regime becomes unstable by increasing driving force), discussion of transition to turbulence is straightforward. Transition usually occurs in the form of a stationary pattern of motion, e.g. cellular convection or secondary flow and undergoes more bifurcations at higher value of the driving force, where the transition value can be well defined according to the flow parameters [1]. A layer of fluid heated from below (Bénard flow) is an example of this successive transition.
Pipe and Plane Couette flow have much more complicated transitional behavior. Despite of their linear stability, finite-amplitude perturbations can trigger a sudden transition to turbulence. Since Osborne Reynolds's seminal paper [2] on the "conditions which determine whether the flow of a fluid is sinuous" in that he described his observations on transition to turbulence in circular pipes, many efforts have been done to explain the transition in linearly stable shear flows. However, the mechanisms which lead to this transition are not completely understood yet. An explicit indication of this ambiguity is the various critical Reynolds numbers ($Re = UL/\nu$ where U, L and ν are the velocity and the length scale of the problem and the kinematic viscosity of the fluid, respectively) specially for pipe flow in fluid dynamics literatures [3]. It was shown that the so-called external flows such as boundary layers or flows around bluff bodies also have similar complex transitional features (Holmes *et al.* [4], Schmid & Henningson [5]). Furthermore, in contrast to supercritical flows where simple vortices and cells emerge, here, one has to deal with complex turbulent structures which spatially and temporally fluctuate. These structures do not persist indefinitely and decay without any precursor or indication (first noted by Brosa [6]) that makes the usage of the statistical approach almost impossible. Recently dynamical system has been

deployed as a complementary approach to explain this transitional behavior [1].

1.2 Turbulence and dynamical system

From the dynamical system point of view, systems have been considered in their state space. Physically, it is the space of all velocity fields, either the perturbations imposed as initial conditions or the basic flow. Mathematically, it is the space that covers all the velocity fields which satisfy the boundary conditions. In this space, velocity can be presented for example by the coefficients of an expansion of velocity fields in a complete basis of orthonormal basis functions [4]. Furthermore, the Navier-Stokes equations in combination with boundary conditions should determine the evolution of the flow and its dynamics at each point of this state in which both laminar profile and turbulent state are contained. In the state space, the laminar profile corresponds to an attractor (a fixed point) that dominates a region in which flow trajectories move toward this attractor. For instance, in pipe flow, the parabolic laminar profile is the attractor toward which all points in its neighborhood (so-called basin) evolve. Assuming turbulent state also as an attractor (Guckenheimer [7]), there is a region in which all initial conditions inside behave chaotically. This chaotic motion, in the form of spatially and temporally fluctuating dynamics, suggests the existence of basic chaotic elements such as horseshoes in turbulent flow (Guckenheimer & Holmes [8]).

1.3 Chaotic saddle model in turbulent flow

Many experimental and numerical studies have been designed in order to find an appropriate model (in dynamical system) for turbulence. The common method, which has been used in both numerical and experimental studies of pipe and Plane Couette flows, is to impose perturbation on basic flow as initial condition to the Navier-Stokes equation and observe its evolution. However, instead of examining on one initial condition and obtaining a long-term solution containing convergent statistical properties, many initial conditions are chosen to be studied and integrated over "intermediate" time, which is necessarily longer than the time that the initial transient is introduced. Since the turbulence has chaotic characteristics, the Lyapunov exponent and its inverse, the Lyapunov time, are the time indicators. Thus the intermediate time is several Lyapunov times long.

These studies have shown that the flow is stable to any perturbation at low Reynolds numbers. This means that the whole state space is occupied by the basin of the laminar attractor, and flow trajectories will asymptote to it independent of their initial positions. By increasing the Reynolds number to some intermediate value (still far from transition), turbulent structures (spots) can be

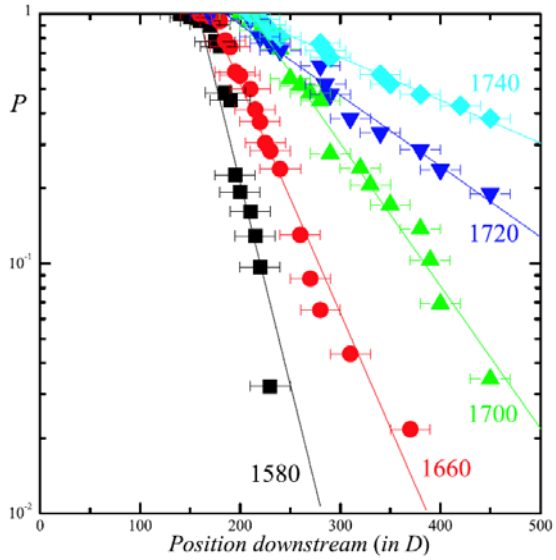

Figure 1.1: Exponential distribution of the lifetimes of turbulent spot (plotted by Peixinho & Mullin [9]). Probability of observation of turbulent spot (so-called puff in pipe flows) versus downstream distance from the point of perturbation for a range of Reynolds numbers (1580–1740). The data are plotted on semi-log scales. The error bars indicate the experimental uncertainty of the measurements.

created by finite-amplitude perturbations, and they decay back to laminar state after an indefinite time. The decay of the turbulent structure has an exponential distribution, and hence the probability of still being turbulent after a time t is $P(t) \sim exp(-\frac{t}{\tau})$, with a characteristic time τ [9, 10, 11] (see Fig 1.1). The possibility of the decay indicates that the state space is not completely occupied by the turbulent attractor. Furthermore, the basin of the turbulent attractor is not compact and flow trajectories can run away toward the laminar attractor. In dynamical systems, the structures which have positive Lyapunov exponents for the motion close to the saddle, but are not persistent are known as chaotic saddles or strange saddles. A chaotic saddle generates transient chaotic dynamics [12, 13]; an orbit enters the basin of the chaotic saddle with its stable manifolds and is influenced by the saddle for some time during which it exhibits chaotic behavior. Then it exits the basin of the saddle along its unstable manifold and eventually enters to the basin of an attracting set such as a fixed point (like the laminar attractor) or a periodic orbit.
The existence of a chaotic saddle has three implications in shear flows [14]:

1. A positive Lyapunov exponent and consequently sensitivity to initial condition.

2. Hyperbolic elements (e.g. coherent structures) appear in the turbulent flow.

3. The distribution of lifetimes of turbulent structure becomes exponential for long times.

Obviously, the study of Lyapunov exponent is only possible in numerical simulations since it is required to follow the time evolution of two states which had close initial conditions. The other two implications have been investigated both numerically and experimentally. Coherent structures such as vortices, streaks, hairpins (Robinson [15]), or traveling waves (Hof *et al.* [16]) have been found in turbulent flows as significant elements each of which occupies a different location in the state space. Thus ideally one would like to identify these structures, study their properties such as frequency and contribution to momentum transport quantitatively and then use them to affect the flows. However, we just limit the explanation to investigation of the last implication, the lifetimes of turbulent structure, which is also investigated in the ongoing thesis.

1.4 Diverging turbulence or transient chaos

Now, the question which needs to be answered is whether the turbulent state remains a transient chaos with increasing Reynolds number, or the flow trajectories will be absorbed by a strange attractor, and the turbulence will sustain itself forever.

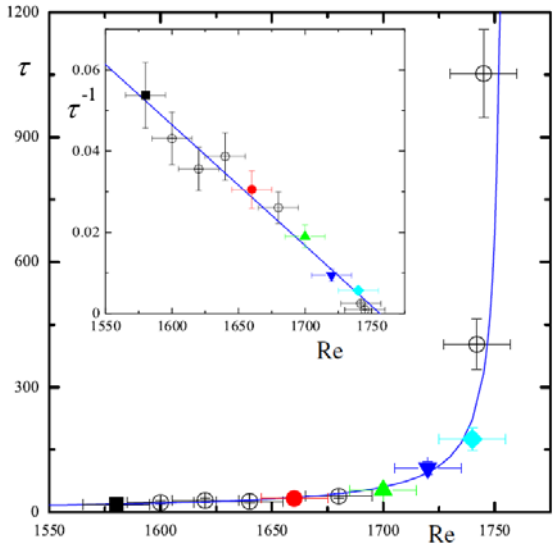

Figure 1.2: Diverging view of turbulence (plotted by Peixinho & Mullin [9]). Variation of the mean decay rate as a function of Re and a fit, which indicates a sharp cut off at $Re \sim 1750 \pm 10$. The inset is the inverse half-life versus Re and a linear fit.

On one hand, some of the experimental and numerical investigations on pipe and Plane Couette flows suggested that the characteristic lifetime of turbulent

spot increases with increasing Reynolds number until it diverges at some critical point [1, 9, 17, 18]; that is, there has to be a form of boundary crisis in the state space where a transition from a chaotic saddle to an attractor happens, and consequently turbulence persists. This is shown in Fig 1.2 where lifetimes (obtained from an experiment in pipe flow) deviate from exponential trend at $Re \sim 1750$. This indicates that the characteristic lifetime, τ, diverges for some finite Reynolds number Re_{cr} for which the turbulent attractor was found to be stable [9].

On the other hand, other studies supported that even though the characteristic lifetime of intermittent state increases with Re, it does not diverge [19, 20, 21]. These latter studies are based on several different experimental set-ups and are consistent with the numerical studies for long pipes and long observation times [22] and present evidence which shows τ increases exponentially with Reynolds number (shown in Fig 1.3). This exponential trend suggests that turbulence is a transitional state which is very long-lived for high Re, rather than being a permanent state, and hence the chaotic repeller model is the correct model for all Re (below the Reynolds number where a global bifurcation occurs). By presuming turbulence as a transitional state which remains dynamically connected with the laminar flow, new possibilities can open up to control turbulence exploiting this connection (using small perturbations [23]).

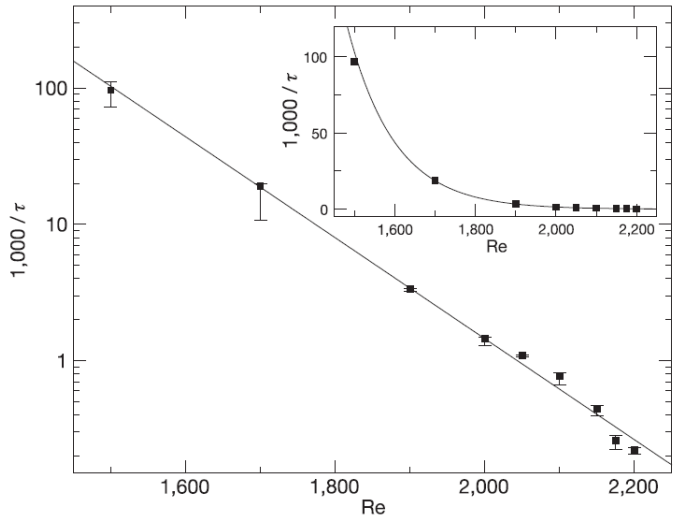

Figure 1.3: Transient turbulence. Characteristic lifetimes obtained from numerical simulation in pipe flow (plotted by Hof *et al.* [19]).

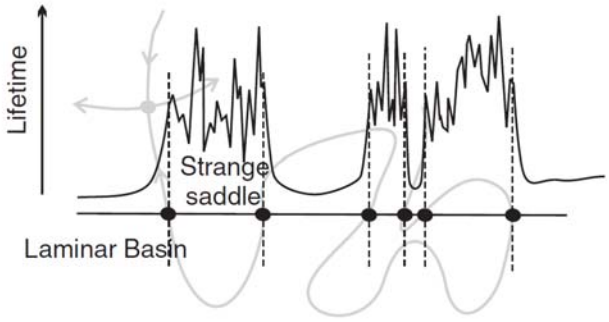

Figure 1.4: Edge of chaos (plotted by Skufca *et al.* [19]). Lifetime changes with the amplitude of perturbation. In laminar basin, lifetime is smooth whereas in saddle region, it appears fractal. The boundary between those behaviors is an edge point. The gray curve illustrates that the behavior on the lifetime is related to structures in state space.

1.5 Edge of chaos

The coexistence of laminar and turbulent state raises the question about their boundaries in state space. One method, which is used in numerical studies to determine this boundary, is perturbing the basic flow many times with different amplitudes of disturbances using an identical initial condition and then examining the lifetime of turbulence [24]. It has been found that variation of lifetime with amplitude is smooth in laminar region whereas lifetimes fluctuate significantly in the basin of chaotic saddles [24] (shown in Fig 1.4). The object which separates these two regions in the state space is called "edge of chaos". It has been shown that for relatively low Reynolds numbers, all the edge points are located on a stable manifold of an invariant structure in the state space [24].

1.6 Transition in Taylor Couette flow

Despite all efforts mentioned above, the variation of the characteristic lifetime with Reynolds number is still a much debated subject, and a uniform conclusion about dynamical behavior of turbulence has not been reached yet. Systems, like pipe and Plane Couette, suffer from contaminated inlet conditions where uncontrolled disturbances enter into the flow. Furthermore, owing to their physical length limitation, a complete life cycle of a turbulent spot can not be observed at high Reynolds numbers, and hence no conclusion can be made about the final state of turbulence. For instance, if we assume that the characteristic lifetime of a turbulent spot in a garden hose is an exponential function of Reynolds number, theoretically a physical length of 40000 km is needed for the spot to decay at $Re = 2400$ [19]. This length is about the circumference of the earth, and practically impossible to observe. Numerical simulations are also problematic in this context since obtaining adequate statistics requires long integration times and a

sufficiently large domain size.

The streamwise periodic characteristic of Taylor Couette flow (which is the flow between two independently rotating concentric cylinders) increases the observation time theoretically to infinity. Furthermore, opposite to open systems like pipe and Plane Couette, no inlet contaminations will be entered to the Taylor Couette flow. Thus it can serve as a proper flow to investigate the lifetime of intermittent state.

The first observation of the lifetime of the turbulent spot in Taylor Couette flow was presented by Borrero-Echeverry & Schatz [25]. They found that the most ideal situation to study the lifetime of intermittent state is when the inner cylinder remains stationary, and consequently the flow is linearly stable. They showed that similar to pipe and Plane Couette flows, the decay of turbulent spot (so-called patch in the Taylor Couette flow) has an exponential distribution (shown in Fig 1.5.a) that is a signature of a Poisson process and supports the chaotic repeller model for shear flows. Furthermore, they found that turbulence is a transient state in this flow even at sufficiently high Reynolds number $Re \sim 9176$. They showed that the characteristic lifetimes increase with Reynolds number faster than exponentially, but do not diverge to infinity (see Fig 1.5.b). Therefore in line with the recent study in pipe flow [19], they suggested a super-exponential function ($\tau(Re)^{-1} = exp(-exp(aRe + b))$ where a and b are constant) to predict the behavior of the characteristic lifetime with increasing Reynolds number.

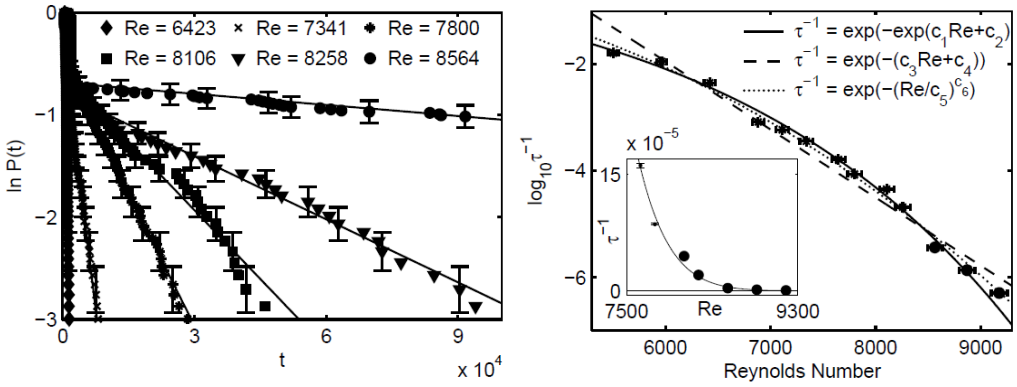

(a) (b)

Figure 1.5: **a)** The probability of observing events whose lifetime is longer than time t decreases exponentially for long times with a decay constant that increases with increasing Re (plotted by Borrero-Echeverry & Schatz [25]). Times are expressed in dimensionless time units $t_{nd} = d/r_o\Omega_o$ where d is the gap between cylinders and r_o and Ω_o are the radius and angular velocity of the outer cylinder. The solid lines show the weighted least squares linear fits the tails of the distributions. **b)** Characteristic lifetime as a function of Re in dimensionless time unit. Horizontal error bars represent absolute error in Re based on experimental limitations. Inset: A plot of τ^{-1} vs. Re on a linear scale shows that $\tau^{-1} \to 0$ only as $Re \to \infty$.

The role of the perturbation type, geometry and boundary condition on the life-

time of the turbulent patch is still unknown. Moreover, other properties of the turbulent patch such as traveling frequency, size and shape have not been studied yet.

1.7 Objectives and outline

The main goal of this thesis is to study the lifetime of the turbulent patch with different perturbation types and boundary conditions in a Taylor Couette flow. A brief introduction to the Taylor Couette flow and its stability is given in chapter 2. In chapter 3, we give a detailed description of the flow facility in which the lifetime measurement is performed. Transition to turbulence in this facility occurs at $Re \sim 6000$, and flow is triggered both locally and globally. We also explain the technique for detection of the turbulent patch from an image. In chapter 4, a 2-d axisymmetric model of the Taylor Couette flow is numerically solved to attain information about the laminar velocity profile, with which a turbulent patch coexists; moreover, a qualitative experiment is performed to verify the results obtained from this numerical simulation.
In chapter 5, the experimental results of the lifetime measurement are presented and discussed. A comparison is made between the results obtained here and the ones reported in the previous study. A universal behavior for the lifetime of the turbulent patch is sought and proper scaling parameters are determined. Furthermore, the role of boundary condition on the lifetime of turbulent patch is examined. Furthermore, various properties of turbulent patch and their dependency on Reynolds number are studied. Finally, conclusions and recommendations of this research are given in chapter 6.

Chapter 2

Taylor Couette flow

2.1 Introduction

Taylor Couette flow, which is the flow between two independently rotating concentric cylinders, has a long and celebrated history (see e.g. Tagg [26] and references therein). This flow is also known as cylindrical Couette flow, circular Couette flow, or rotating Couette flow. Like all other Couette-type flows, it is driven by the movement of the walls that bound a viscous fluid. Taylor Couette flow is mostly known for a transition preceded by a hierarchy of bifurcations that is caused by centrifugal instabilities [27, 28].

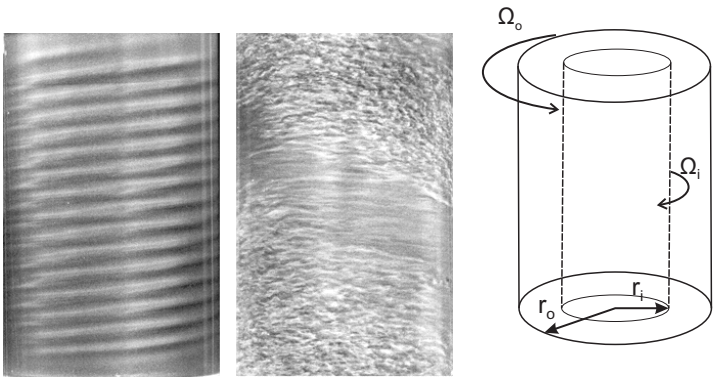

(a) (b)

Figure 2.1: Taylor Coutte flow. **a)** The onset of instability of flow between counter-rotating cylinders in a Taylor Couette system (left). At much higher rotation rates, the flow develops turbulent helical bands that alternate with bands of laminar flow (right). Images courtesy of Professor Harry Swinney. **b)** Schematic figure of Taylor Couette set-up. r_i and r_o are the radii, Ω_i and Ω_o are the angular velocities of the inner and the outer cylinders, respectively.

2.2 Taylor Couette flow application

Two flows with different values of length scales, flow velocities, or fluid properties can still exhibit the same dynamics. According to the principle of dynamic similarity, all flows with the same governing equations and control parameters show the same dynamic behavior. Many prototypes have been built based on this principle to model flows in which conducting a test is very expensive or even impossible. One good example is modeling astrophysical and geophysical rotating shear flows for which the Taylor Couette device can be used as an excellent prototype [29]. Furthermore, the Taylor Couette flow is potentially rich with stability properties and has geometrical properties which make it suitable for investigating the lifetimes of turbulent structures (as mentioned in chapter 1.6); therefore, many experimental and numerical works have been dedicated to this flow. Here, a brief introduction to different aspects of the Taylor Couette flow from governing equations to stability analysis have been given to make the reader acquainted with the general properties of this flow.

2.3 Flow regimes in Taylor Couette system

A wide range of flow regimes can be obtained in Taylor Couette system depending on the angular velocity of the inner and the outer cylinders. Following the work

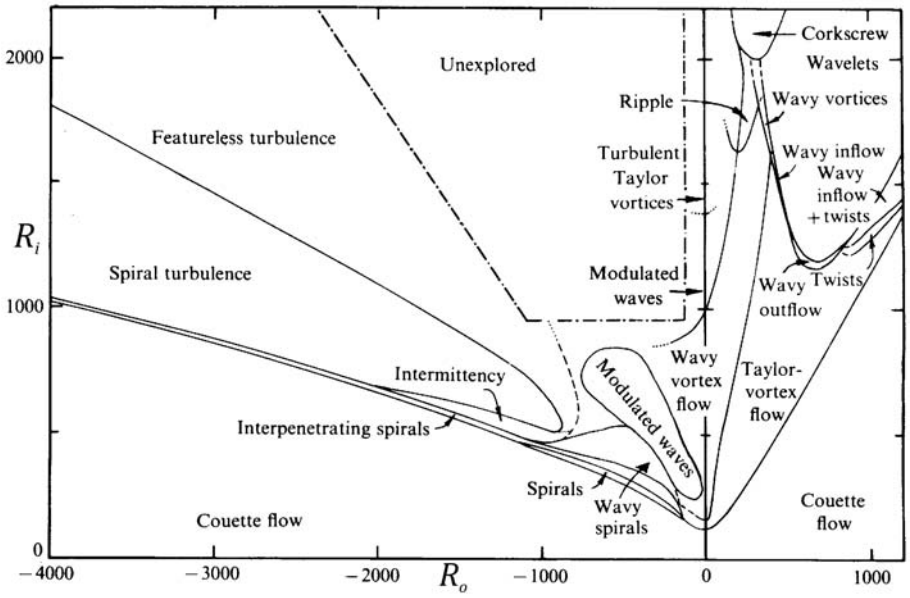

Figure 2.2: Flow regimes observed in Taylor Couette set-up at different inner and outer Reynolds number (plotted by Andereck [27]). Dashed lines indicate transition boundaries that are difficult to establish from visual observation alone since there is no abrupt change in appearance. Dotted lines indicate expected, but not yet observed, continuation of several boundaries.

of Coles [28], who discovered up to 26 stable flow states at the same Reynolds number (that showed the dependency of the states on the path followed in parameters space), Andereck [27] performed a complete experimental investigation on flow states in a Taylor Couette system that provided a coherent characterization of flow states and transition between them. He explored various flow regimes in the system (shown in Fig 2.2).

2.4 Governing equations

As in all incompressible Newtonian flows, the governing equations for the Taylor Couette flow are the Navier-Stokes equations [29]:

$$\begin{aligned} \frac{d\mathbf{u}}{dt} + \mathbf{u}.\nabla\mathbf{u} &= -\frac{1}{\rho}\nabla p + \nu\nabla^2\mathbf{u}, \\ \nabla.\mathbf{u} &= 0 \end{aligned} \tag{2.1}$$

where ρ is density of the fluid, $\mathbf{u}$ is velocity and p is pressure (gravity force is included in pressure term).

2.5 Control parameters

Independent non-dimensional parameters have been defined such that they can fully characterize the flow. This can be done in two different ways: a traditional choice and a dynamics motivated choice.

2.5.1 Traditional choice

In this approach, geometrical properties of the flow are considered. The gap between the cylinders d and the diffusion time $t = d^2/\nu$ have been chosen as the length and time scales of the flow. The generally accepted non-dimensional parameters are radius ratio η and the Reynolds numbers of the inner and outer cylinders defined as:

$$\begin{aligned} \eta &= \frac{r_i}{r_o}, \\ R_i &= \frac{r_i\Omega_i d}{\nu}, \\ R_o &= \frac{r_o\Omega_o d}{\nu}. \end{aligned} \tag{2.2}$$

2.5.2 Dynamics motivated choice

In order to distinguish the role of different forces existing in the flow, a more dynamical approach is required in which each non-dimensional parameter represents a particular characteristic of the flow. The equation of motion is written

in a rotating frame with the arbitrary angular velocity Ω_{rf} instead of an inertial frame (i.e. $\phi = \theta - \Omega_{rf}t$ and $\mathbf{w} = \mathbf{u} - \Omega_{rf} r e_\phi$ where θ and ϕ are the azimuthal coordinates in the inertial and rotating frame respectively). Again d is chosen as unit length, and the inverse of a typical shear $\tilde{S}$ and $\tilde{r}$ are chosen as unit time and a typical radius, respectively. By defining the "advection shear term*" in cylindrical coordinates (r, ϕ, x) as (proposed in [30, 31]):

$$\mathbf{w}.\nabla'\mathbf{w} = \mathbf{w}.\nabla(w_r\mathbf{e_r}) + [r\mathbf{w}.\nabla(\frac{w_\phi}{r})]\mathbf{e_\phi} + \mathbf{w}.\nabla(w_x\mathbf{e_x}) \tag{2.3}$$

equation (2.1) takes a new form:

$$\begin{gathered}\frac{d\mathbf{w}}{dt} + \mathbf{w}.\nabla'\mathbf{w} = -\nabla\Pi - R_\Omega\mathbf{e_x}\times\mathbf{w} + R_c(\frac{w_\phi^2}{r/\tilde{r}}\mathbf{e_r}) - R_c(\frac{w_\phi w_r}{r/\tilde{r}}\mathbf{e_\phi}) + Re^{-1}\nabla^2\mathbf{w}, \\ \nabla.\mathbf{w} = 0,\end{gathered} \tag{2.4}$$

where

$$\begin{aligned} Re &= \frac{\tilde{S}d^2}{\nu}, \\ R_\Omega &= \frac{\Omega_{rf}}{\tilde{S}}, \\ R_c &= d/\tilde{r}. \end{aligned} \tag{2.5}$$

Re, R_Ω and R_c are the dynamics motivated control parameters. The influence of shear is measured by shear Reynolds number (Re). R_c is curvature number and indicates the effect of cylinder curvature in the flow. R_Ω is rotation number and represents the effect of rotation in the flow. It has to be noted that the centrifugal term produced by the rotating frame is subtracted to the pressure term and forms the modified pressure Π.

As mentioned earlier, Ω_{rf} has been chosen arbitrarily. For the sake of the simplicity of the notation and preserving the symmetry, one can choose Ω_{rf} so that $w_\theta(r_i) = -w_\theta(r_o)$. This definition of Ω_{rf} amounts to fixing $\tilde{r}$ by $\Omega(\tilde{r}) = u_\theta(\tilde{r})/\tilde{r} = \Omega_{rf}$. The typical shear can be described at the same location $\tilde{S}(\tilde{r})$. With these definitions, one can show that the relation between the traditional and motivated control parameters are as follows:

$$\begin{aligned} Re &= \frac{\tilde{S}d^2}{\nu} = \frac{2}{1+\eta}|\eta R_o - R_i|, \\ R_\Omega &= \frac{2\Omega_{rf}}{\tilde{S}} = (1-\eta)\frac{R_i + R_o}{\eta R_o - R_i}, \\ R_c &= \frac{1-\eta}{\eta^{1/2}}. \end{aligned} \tag{2.6}$$

*By introducing the advection shear, mean flow derivative and global curvature contributions to the advection term can be separated. This modified advection term shows its importance especially in the case of solid body rotation where the shear vanishes while the advection still exists due to the global curvature [30].

where $\tilde{r} = \sqrt{r_i r_o}$. These control parameters are applicable to all shear rotating flows, e.g. Plane Couette flow is a special case where the curvature effect tends to zero (i.e. $\lim R_c \to 0$).

2.6 Stability analysis of Taylor Couette flow

Transition to turbulence is a form of instability developing in a flow. Thus in order to have a better understanding of transition, it is necessary to know the stability properties of the flow. Here, a short summary of previous works on stability in Taylor Couette flow is given.

The classification of stability analysis differs depending on the type of disturbances imposed on the basic flow. Linear stability analysis examines the effect of infinitesimal perturbations on the flow and determines whether the equations of motion demand that perturbations should grow or decay in time. In this analysis, the problem is linearized by neglecting the quadratic and higher order terms in the perturbation variables and their derivatives [32]. However, a real flow may be stable to the infinitesimal disturbances (linearly stable), but still can be unstable to sufficiently large disturbances (non-linearly unstable). This is the topic of non-linear stability. In this respect, flows are generally categorized into two classes: subcritical and supercritical [29]. Subcritical flows are linearly stable and become unstable by imposing finite-amplitude perturbations whereas supercritical flows are destabilized by the infinitesimal disturbances. In the following, first linear stability is discussed, and then non-linear stability in subcritical flows is explained.

Late in nineteenth century, Rayleigh discovered a criterion which determined necessary and sufficient conditions for instability in the Taylor Couette flow. Assuming inviscid flow, he utilized Kelvin theorem to obtain a stability criterion. According to his work, the marginal stability threshold is $R_\Omega^{\infty-} = -1$ and $R_\Omega^{\infty+} = 1/\eta - 1$ where R^∞ is the limit inviscid case. The plus and minus superscript signs are for the cyclonic ($R_\Omega > 0$) and the anti-cyclonic ($R_\Omega < 0$) regimes, respectively. Rayleigh did not consider three important factors in his work:

1. The effect of the non-symmetric perturbations inside the flow, which can have more impact than the axisymmetric ones.

2. Viscosity acts as a damping force on the flow and increases the domain of linear instability.

3. Stability to the infinitesimal perturbations does not imply that the flow is necessarily stable to the finite-amplitude perturbations.

Following his work, Taylor deployed the classical normal mode analysis to study stability of the flow. He showed that viscosity can behave as a stabilizing force

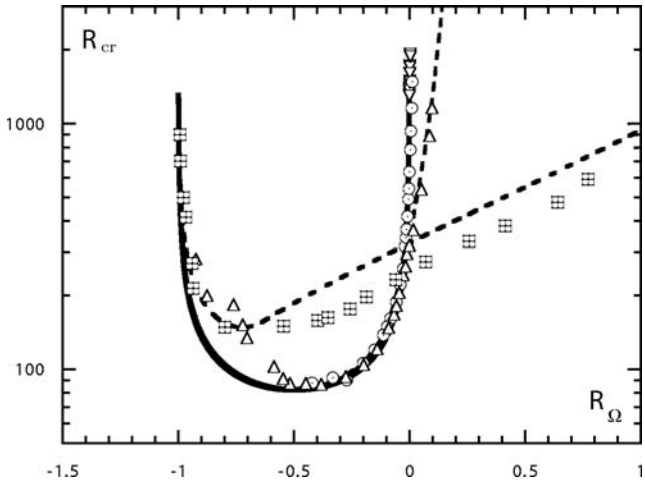

Figure 2.3: Linear stability boundary (plotted by Longaretti *et al.* [29]). Critical Reynolds number Re_{cr} is plotted as a function of rotation number R_Ω. Numerical data by Snyder [33] $\boxplus$ for $\eta = 0.2$, $\triangle$ for $\eta = 0.8$, and $\odot$ for $\eta = 0.935$. Experimental data by Prigent *et al.* [34] $\triangledown$ for $\eta = 0.983$. Continuous line: Lezius & Johnston [35] Plane Coutte or small gap limit stability criteria. Dashed line: Esser and Grossman [36] prediction for $\eta = 0.8$ and $\eta = 0.2$.

damping the perturbations. More comprehensive analytical work was done by Esser and Grossman [36], including the non-axisymmetric modes, led to the results that were consistent with the linear stability theory and experiments. Fig 2.3 demonstrates critical Reynolds number as a function of R_Ω and η where the numerical work of Snyder [33] indicates the dependency of critical Reynolds number on the geometry of the flow (i.e. radius ratio).

In order to study stability properties of the subcritical flows, one has to deal with the finite-amplitude perturbations and their effects on the flow. Analyzing the effects of these perturbations are different from the effects of infinitesimal ones. The infinitesimal perturbations absorb the energy from the basic flow whereas the large perturbations are fed by an ultimate external energy source which has the same level of energy as the basic flow. The meaning of instability itself becomes hard to understand when the perturbations and the basic flow are at the same energy level.

In the lack of a general theory to examine transition to turbulence in the subcritical flows, experiments have been conducted to determine the non-linear stability boundary. The most common methods used in the experiments to find these boundaries are: 1) torque measurement, 2) flow visualization, and 3) mean velocity profile measurement. Fig 2.4 illustrates the non-linear stability boundary where the critical Reynolds number shows a large dependency on the rotation number. To find a global manifold for the dependency of the critical Reynolds number on the rotation number, one can use the results from Taylor experiment (indicated by triangles in Fig 2.4). However, it is limited to the case where the inner cylinder is at rest (which is the state of our interest), and the role of the

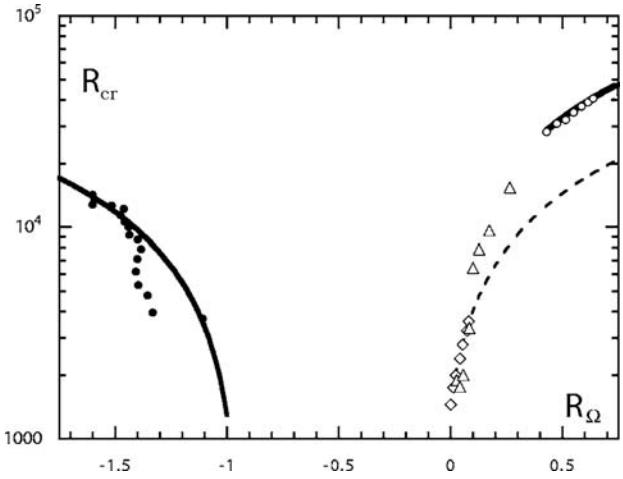

Figure 2.4: Non-linear stability boundary in Taylor Couette flow (By Longaretti *et al.* [29]). Critical Reynolds number Re_{cr} is plotted as a function of rotation number R_Ω. $\triangle$: data of Taylor [34, 37] for $0.7 < \eta < 0.935$ where inner cylinder is at rest, $\circ$: data of Richard [33] for $\eta = 0.7$ where $R_\Omega > 0.5$,$\Diamond$: data of Tillmark [38] for rotating Plane Couette flow $\eta = 1$ where $R_\Omega > 0$, dotted line: linear fit of Tillmark's data, plain line: linear fit of Richard's data. $\bullet$: data of Richard for $\eta = 0.7$ where -1.5< R_Ω <-1, plain line: linear fit of Richard's data.

inner cylinder rotation is not considered. Unfortunately, data available from the Taylor experiment is read from the original figure that naturally causes some error in determination of the critical Reynolds number. One of the fits through the Taylor data points is proposed by Richard & Zahn [33] as:

$$Re_{cr}(\eta) = 1400 + 550000(1 - \eta)^2 \tag{2.7}$$

which can be used as an estimate for the critical Reynolds number.

Chapter 3

Experimental set-up

3.1 Introduction

In this chapter a brief description of the experimental set-up is given. The procedure to disturb the laminar flow and create the turbulent patch is described. Finally the method of measuring the lifetime of the turbulent patch is explained.

3.2 Taylor Couette set-up

The experimental apparatus consists of two vertical concentric cylinders, which are made of plexiglass and can rotate independently of each other (Fig 3.1). Both the inner and the outer cylinders are connected to two independent Brushless DC motors (Maxon,250W), which can rotate up to 10 Hz with an absolute precision of ± 0.01 Hz. A HBM torque meter (T20WN, 2N.m) is connected to the inner cylinder through the driving shaft. Inner and outer radii of the cylinders are $r_i = 110 \pm 0.05$ mm and $r_o = 120 \pm 0.05$ mm. The outer cylinder is attached to the top and bottom lids, and there are gaps (1.5 mm) between the end surfaces of the inner cylinder and the lids. The height of the inner cylinder is $L = 220$ mm, and the gap between two cylinders is $d = r_o - r_i = 10$ mm. According to these geometrical properties, two non-dimensional numbers are defined: aspect ratio $\Gamma = L/d = 22$ and radius ratio $\eta = r_i/r_o = 0.917$.
Distilled water is used as working fluid with the viscosity of $\nu = 1.004 \times 10^{-6}$ at the temperature T$= 20°$C.

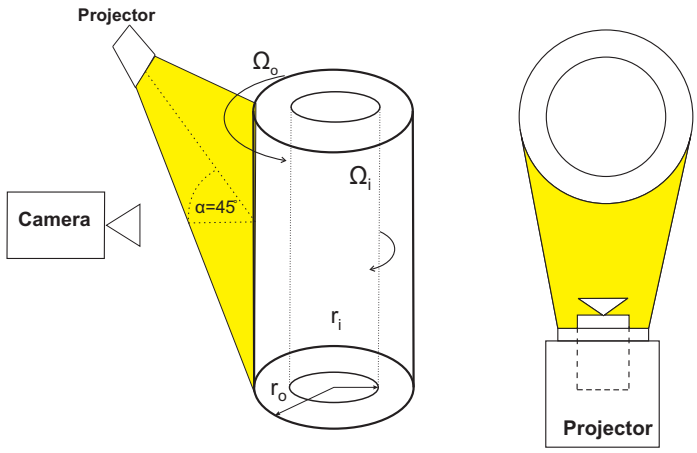

Figure 3.1: Schematic figure of the Taylor Couette set-up. Figure (a) and (b) show the set-up in the side and top views.

3.3 Flow visualization

The most common way to visualize the flow structures in the Taylor Couette flow is to use Kalliroscope flakes [25, 27, 39]. They are the suspensions of microscopic crystalline platelets. When these flakes are put into motion, the suspended platelets orient so as to align their larger dimensions parallel to the planes of shear [40]. In the presence of incident light, areas of varying alignment reflect differing intensities of light. Turbulent fluctuation of the flow velocity leads to fluctuation of the alignment of the platelets and consequently variation of the light intensity in turbulent areas that makes the turbulent patch distinguishable from the laminar background. It has been shown that this intensity is related to the radial velocity component of the flow [39].

Since this material was not available, Iriodin pigments (Iriodin 121), which have similar properties as Kalliroscope particles, were mixed with water to visualize the flow. The low value of concentration, 0.007 % volume, was chosen to prevent any significant change in the water properties such as density and viscosity. To illuminate the particles, the cylinders were exposed to white light from a projector. Owing to having curvature in the geometry, straight illumination caused specular reflection. Hence the flow was illuminated with an oblique angle with the axis of the cylinders (Fig 3.1.a).

3.4 Measurement procedure

As mentioned in previous chapters, the Taylor Couette flow with stationary inner cylinder is linearly stable, and therefore, sudden transition occurs at sufficiently high Reynolds number [1]. In our Taylor Couette set-up, spontaneous transition happens at $Re_{cr} \sim 6000^*$, and hence lifetime measurements were conducted for Reynolds numbers below this value. As the first step, laminar flow had to be generated. This was done by slowly accelerating the outer cylinder up to a certain frequency (corresponding to a desired Reynolds number) while the inner cylinder was at rest. After reaching this frequency, the system was allowed to run for 100 seconds ($\sim$1 radial diffusion times $t_d = d^2/\nu$) to rule out any transient. Since the temperature of the water and consequently its viscosity fluctuated during the experiment, it was necessary to measure the temperature regularly (either after 5 runs or 600 seconds) and accordingly correct the Reynolds number by changing the frequency of the outer cylinder.
In order to trigger the transition, two different methods were employed: global perturbation and local perturbation. In the former method, the flow was perturbed by sudden acceleration of the inner cylinder up to 0.65 Hz in the opposite direction of the outer cylinder. The inner cylinder was remained rotating at this frequency for 3 seconds and then immediately stopped. It was observed here and in the previous study [25] that as long as the perturbation triggers the transition to the intermittent state, the lifetime of the turbulent patch does not depend on the strength or duration of the perturbation. Thus in all experiments, the flow was disturbed by the same inner cylinder frequency. In the latter method, the turbulent patch was created by simultaneous injection and suction of water for 1 sec through two 0.9 mm holes located on the half height of the inner cylinder. In order to have a small localized perturbation, two holes were placed at a distance of 43 mm from each other. This method has also been used in pipe flow to create turbulent structures [9, 19].
A CCD camera with frame rate of 10 Hz and resolution of 500x2800 pixels, which corresponded to 37.5x200 mm in physical space, was used to capture the flow. Post-processing was required to extract useful information from each image. Depending on what property of the turbulent patch was to be examined, different processing steps had to be taken.

*The critical Reynolds number in our system was measured as follow: the laminar flow was generated at the outer cylinder frequency of 0.53 Hz (corresponding to Re=4000) while the inner cylinder was at rest. The system was allowed to run for 100 seconds (that is the radial diffusion time t_d). If the flow became turbulent after this time, the Reynolds number was considered as the critical one, otherwise the frequency of the outer cylinder was increased by df_{cyl}=0.01 Hz, and the flow was checked again. This procedure was repeated till the transition to turbulence occurred.

3.4.1 Lifetime measurement

The aim was to determine the lifetime of the turbulent patch from the gray-scale images recorded after disturbing the flow. In order to rectify the image, each image was subtracted and normalized by the average of one hundred images taken from the laminar flow (denoted by I_{avg}). Then different properties of the rectified image such as the cumulative sum, mean and standard deviation were examined in order to find an indication of the patch. It was found that the standard deviation of the image matrix is the best indication for the existence of the patch, thus N was defined as:

$$N = std(\frac{I - I_{avg}}{I_{avg}}), \tag{3.1}$$

where *std* is the standard deviation function. N was sequentially calculated for each image and compared with a threshold, which had been defined empirically. If N remained smaller than the threshold for 40 consecutive images (4 seconds), the last image with N higher than the threshold was chosen as the image where the patch was last observed. N is illustrated as a time series in Fig 3.2 where it is clearly seen that the amplitude of the signal dramatically drops at $t = 205$ sec, that is thus the time the patch disappeared. The accuracy of this approach was verified by hand for some random runs.

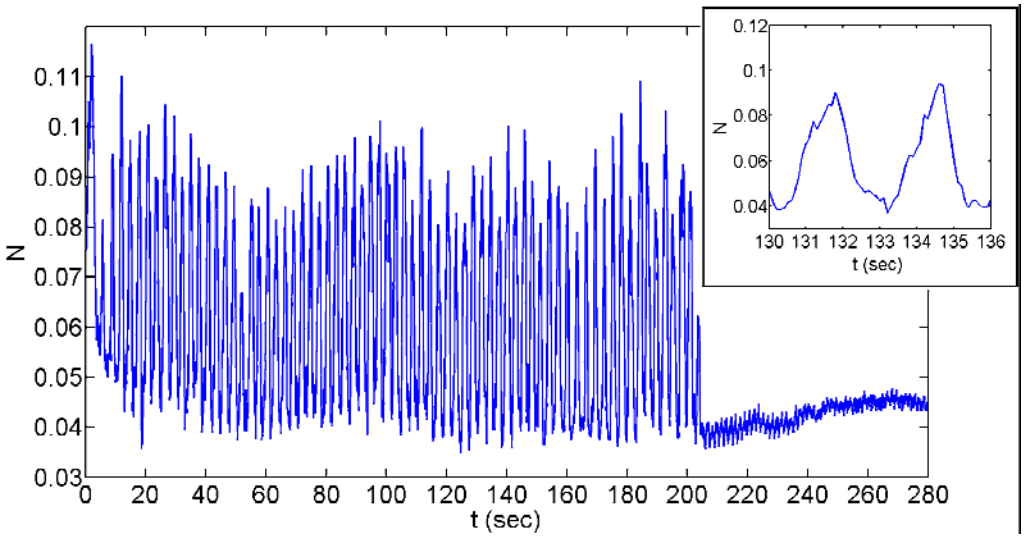

Figure 3.2: Standard deviation of the normalized image matrix as a time series. The turbulent patch is created by global perturbation at $Re = 4530$. Inset, zoom-in on the signal. Peaks corresponds to a situation when all or most of the patch is in front of the camera while troughs corresponds to a situation when patch is rotated away and the laminar back ground is in the direction of the camera. The distance between the two peaks indicates the time that patch makes a complete round.

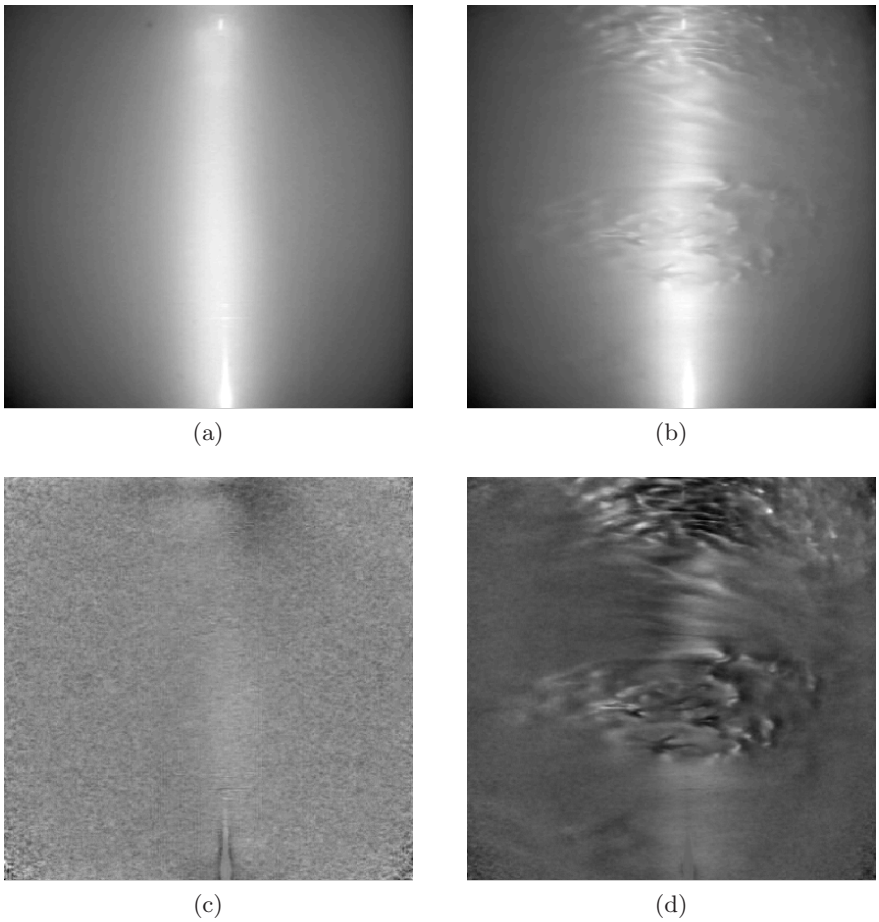

(a) (b)

(c) (d)

Figure 3.3: Images of Taylor Couette flow at $Re = 4530$. Figure (a) is an image of a laminar flow whereas image (b) shows the coexistence of a turbulent patch with laminar background. Figure (c) and (d) are the normalized images of (a) and (b).

3.4.2 Distinguishing turbulent patch from laminar background

In order to distinguish the turbulent patch from the laminar flow, the flow state in each pixel of the image matrix had to be determined. Fig 3.3.b shows an image of a turbulent patch coexisting with a laminar flow. As it is seen in the figure, pixels around the center (bright areas) and near the corners (dark areas) of the image suffer from high and low light intensities that may cause a loss of information about the patch in these areas. Therefore, a strip of the image, sufficiently far from both areas where there is a proper light intensity, was cut out to be examined. To convert the image of the strip to a binary matrix, where laminar and turbulent regions corresponds to zeros and ones respectively, following procedure was performed. We defined α as:

$$\alpha = |\frac{I_{st} - I^{st}_{avg}}{I^{st}_{avg}}| * 100. \tag{3.2}$$

(where I_{st} and I_{avg}^{st} are the strip image matrix and the corresponding mean image matrix) indicating the percentage of the difference between the light intensity in the image and the mean matrix. If α was higher than the threshold, $\alpha \geq 16$, the pixel is assigned to one, otherwise to zero. This threshold was determined by examining two images from a fully laminar and a fully turbulent flow (Fig 3.4). The threshold had to be defined in such a way that led to the minimum and the maximum number of turbulent pixels in the fully laminar and the fully turbulent image, respectively. Therefore, function f was introduced as the signal to noise ratio:

$$f(\alpha) = \frac{(100 - R_L) + R_T}{(100 - R_T) + R_L}, \tag{3.3}$$

(where R_L and R_T are the percentage of the turbulent pixels in the fully laminar and the fully turbulent images) that indicates the goodness of the chosen threshold. This function reaches its maximum value at $\alpha = 16$ (shown in Fig 3.4 inset), and hence this value was chosen as the threshold between the laminar and the turbulent state in the image.

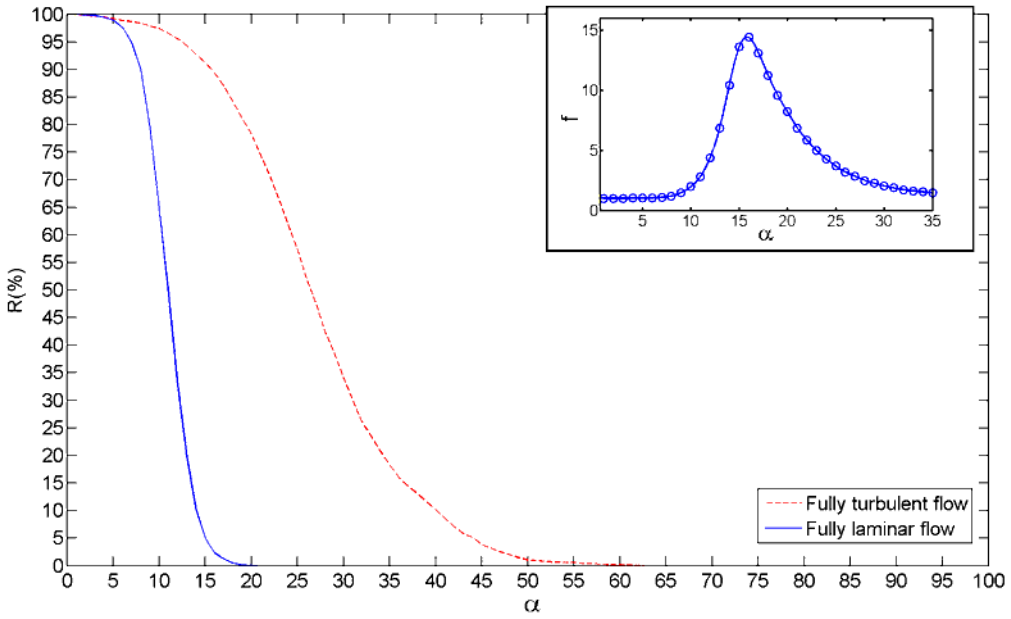

Figure 3.4: Threshold to distinguish the laminar region from the turbulent patch in the image matrix. R indicates the percentage of the pixels in which α is higher than threshold and the flow is considered as turbulent. Inset, the signal to noise ratio function f versus the threshold α.

After converting the image matrix to a binary matrix, different information about the turbulent patch such as size and vertical position are obtainable. For example, if a center column of the binary matrix is cut out and attached to the same column of next image and this is repeated for all images, a time series of the vertical position of the patch will be achieved.

Chapter 4

Laminar velocity profile in Taylor Couette flow

4.1 Introduction

The purpose of this chapter is to study the laminar flow in the Taylor Couette set-up with stationary inner cylinder using numerical simulation. In order to have a comprehensive understanding of the behavior of the turbulent patch, the laminar flow with which the patch coexists, also has to be understood; therefore, experimental measurement or numerical simulation has to be performed to investigate the laminar flow. Owing to the geometrical properties of the set-up (e.g. curvature and small gap), implementing measurement techniques such as PIV and LDV is difficult and time consuming. Thus numerical simulation (CFD) is performed on a geometry similar to that of the experimental set-up, and then a qualitative experiment is conducted to verify the general aspects of the numerical results.

4.2 Problem description

Flow is simulated in a 2-d axisymmetric model of the Taylor Couette set-up shown in Fig 4.1. Flow occurs in the area between the cylinders that is indicated by blue in the figure. The working fluid is water and its temperature is taken as 20°C. The outer cylinder is rotating at 3.34 rad/s (corresponding to $Re = 4000$) while the inner cylinder is at rest. The velocity and pressure of the interior domain are the unknowns and have to be determined. First, the problem is solved for the set-up completely filled with water, and then the partially-filled system is solved.

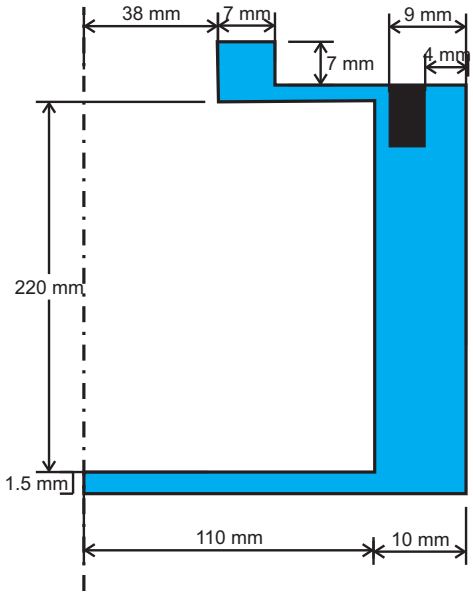

Figure 4.1: 2-d model of the Taylor Couette set-up. Blue area is where the flow occurs, and the black rectangle is a metal piece attached to the top lid (and will be named as barrier). The black dashed-dotted line represents the axis of symmetry.

4.3 Governing equations and dynamic solution

The intent here is to attain a primary analytical solution from the governing equations that will be used later on to justify the results of the numerical simulation. In order to have a better understanding of the problem, the flow domain is divided into two main regions: flow between the inner cylinder and the end-walls (so-called Von Kármán region), and flow between the inner and outer cylinder walls (so-called Taylor Couette gap).

4.3.1 Von Kármán gap

In the Von Kármán region, the situation is similar to a flow contained between two finite rotating discs where the axis of rotation is normal to disc surfaces. Assuming an incompressible Newtonian fluid, the Navier-Stokes equations in cylindrical coordinate (r,θ,x) are:

$$\begin{aligned}
&\frac{\partial u_r}{\partial t} + u.\nabla u_r - \frac{u_\theta^2}{r} = -\frac{1}{\rho}\frac{\partial p}{\partial r} + \nu\left(\nabla^2 u_r - \frac{u_r}{r^2} - \frac{2}{r^2}\frac{\partial u_\theta}{\partial \theta}\right),\\
&\frac{\partial u_\theta}{\partial t} + u.\nabla u_\theta + \frac{u_r u_\theta}{r} = -\frac{1}{\rho}\frac{\partial p}{r\partial \theta} + \nu\left(\nabla^2 u_\theta + \frac{2}{r^2}\frac{\partial u_r}{\partial \theta} - \frac{\partial u_\theta}{\partial r^2}\right),\\
&\frac{\partial u_x}{\partial t} + u.\nabla u_x = -\frac{1}{\rho}\frac{\partial p}{\partial x} + \nu\nabla^2 u_x,\\
&\frac{\partial u_x}{\partial x} + \frac{1}{r}\frac{\partial (r u_r)}{\partial r} + \frac{1}{r}\frac{\partial u_\theta}{\partial \theta} = 0
\end{aligned} \tag{4.1}$$

where

$$u.\nabla = u_r\frac{\partial}{\partial r} + \frac{u_\theta}{r}\frac{\partial}{\partial \theta} + u_x\frac{\partial}{\partial x},$$
$$\nabla^2 = \frac{1}{r}\frac{\partial}{\partial r}\left(r\frac{\partial}{\partial r}\right) + \frac{1}{r^2}\frac{\partial^2}{\partial \theta^2} + \frac{\partial^2}{\partial x^2}. \tag{4.2}$$

Boundary conditions are given in Table 4.1 where h is the gap between the inner and the outer cylinder end-walls. Assuming steady axisymmetric flow, the initial

	u_r	u_θ	u_x
$x = 0$	0	$r_o\Omega_o$	0
$x = h$	0	0	0

Table 4.1: Velocity components at boundaries

solution which satisfies the boundary conditions (kinematic solution) is:

$$u_r = 0, \qquad u_\theta = r_o\Omega_o(1 - \frac{x}{h}), \qquad u_x = 0. \tag{4.3}$$

However, the dynamics of the flow is not considered in this solution. By non-dimensionalizing the governing equations, the dominant forces in the flow are determined (and therefore, the dynamic solution is obtained). Using the characteristic velocity and length scales of the flow, the following non-dimensional variables are defined:

$$r^* = \frac{r}{r_o}, \qquad x^* = \frac{x}{h}, \qquad p^* = \frac{p}{\rho r_o^2\Omega_o^2},$$
$$u_r^* = \frac{u_r}{r_o\Omega_o}, \qquad u_\theta^* = \frac{u_\theta}{r_o\Omega_o}, \qquad u_x^* = \frac{u_x}{h\Omega_o}. \tag{4.4}$$

Substitution of these variables in equation (4.1) in radial direction gives:

$$u_r^*\frac{\partial u_r^*}{\partial r^*} + u_x^*\frac{\partial u_r^*}{\partial x^*} - \frac{u_\theta^{*2}}{r^*} = -\frac{\partial p^*}{\partial r^*} + \frac{1}{Re_h}\left[\gamma^2(\frac{\partial^2 u_r^*}{\partial r^{*2}} + \frac{1}{r^*}\frac{\partial u_r^*}{\partial r^*} - \frac{u_r^*}{r^{*2}}) + \frac{\partial^2 u_r^*}{\partial x^{*2}}\right]. \tag{4.5}$$

with the non-dimensional parameters:

$$\gamma = \frac{h}{r_o}, \qquad Re_h = \frac{h^2\Omega_o}{\nu}. \tag{4.6}$$

Here $\gamma^2 << 1$, thus equation (4.5) simplifies to:

$$u_r^*\frac{\partial u_r^*}{\partial r^*} + u_x^*\frac{\partial u_r^*}{\partial x^*} - \frac{u_\theta^{*2}}{r^*} = -\frac{\partial p^*}{\partial r^*} + \frac{1}{Re_h}\frac{\partial^2 u_r^*}{\partial x^{*2}}. \tag{4.7}$$

For small Reynolds numbers ($Re_h << 1$), the last term in equation (4.7) becomes dominant which means the flow is highly affected by the viscous forces; thus the resulting dynamic solution is equal to the kinematic solution. However, the Reynolds number of the flow studied here is of the order of unity; therefore,

pressure and inertial forces are also involved in the dynamics of the flow. To find an analytical solution including these forces, classical perturbation theory is utilized where solutions are expressed in a power series in terms of the scaling parameter Re_h (as suggested by Delfos [41]); therefore, the velocity components and pressure are written as:

$$\begin{aligned} u_r^* &= u_{r,0}^* + Re_h.u_{r,1}^* + Re_h^2.u_{r,2}^* + ... \\ u_\theta^* &= u_{\theta,0}^* + Re_h.u_{\theta,1}^* + Re_h^2.u_{\theta,2}^* + ... \\ u_x^* &= u_{x,0}^* + Re_h.u_{x,1}^* + Re_h^2.u_{x,2}^* + ... \\ p^* &= p_0^* + Re_h.p_1^* + Re_h^2.p_2^* + ... \end{aligned} \tag{4.8}$$

The necessary and sufficient condition for the convergence of each series is:

$$\lim_{n\to\infty} Re_h|u_{n+1}^*|/|u_n^*| < 1$$

where $|u_n^*|$ is the magnitude of the nth velocity component in each series. Using the kinematic solution for $u_{r,0}^*,\ u_{\theta,0}^*,\ u_{x,0}^*,\ p_0^*$ and substituting them into equation (4.7) (considering first order approximation), we obtain:

$$Re_h^2\left(u_{r,1}^*\frac{\partial u_{r,1}^*}{\partial r^*} + u_{x,1}^*\frac{\partial u_{r,1}^*}{\partial x^*}\right) - \frac{u_{\theta,0}^{*2}}{r^*} = -\frac{\partial p_1^*}{\partial r^*} + \frac{\partial^2 u_{r,1}^*}{\partial x^{*2}}. \tag{4.9}$$

Now we examine the advection term in the left hand side of equation (4.9). The order of each term is estimated by:

$$\begin{aligned} Re_h^2 u_{r,1}^*\frac{\partial u_{r,1}^*}{\partial r^*} &\sim Re_h^2 u_{n+1}^{*2}, \\ Re_h^2 u_{x,1}^*\frac{\partial u_{r,1}^*}{\partial x^*} &\sim Re_h^2 u_{n+1}^{*2}, \\ -\frac{u_{\theta,0}^{*2}}{r^*} &\sim u_n^{*2}. \end{aligned} \tag{4.10}$$

Based on the condition for the convergence of the series, $Re_h|u_{n+1}^*|/|u_n^*| < 1$, the centrifugal term is larger than two other terms, i.e. $u_n^{*2} > Re_h^2 u_{n+1}^{*2}$. Considering the centrifugal force as the dominant advection term and neglecting the other advection terms, the momentum equation in the radial direction becomes:

$$-\frac{u_{\theta,0}^{*2}}{r^*} = -\frac{\partial p_1^*}{\partial r^*} + \frac{\partial^2 u_{r,1}^*}{\partial x^{*2}}. \tag{4.11}$$

Hence flow is dominated by three forces; namely, centrifugal and viscous forces, and pressure gradient.

There are two unknowns in equation (4.11) which have to be determined: the radial velocity $u_{r,1}^*$ and the pressure gradient. The integral of the radial velocity over the height of the gap is zero (which can easily be shown assuming a control

volume with one edge at axis of symmetry); therefore, it is just a matter of integration to obtain the pressure gradient from equation (4.11):

$$\frac{\partial p_1^*}{\partial r^*} = \frac{3}{10} r^*$$

Substituting the pressure gradient into equation (4.11), the radial velocity becomes:

$$u_{r,1}^* = r^*(\frac{6}{60}x^* - \frac{21}{60}x^{*2} + \frac{20}{60}x^{*3} - \frac{5}{60}x^{*4}), \tag{4.12}$$

and the axial velocity is obtainable from the continuity equation as:

$$u_{x,1}^* = (\frac{6}{60}x^{*2} - \frac{7}{60}x^{*3} + \frac{5}{60}x^{*4} - \frac{1}{60}x^{*5}). \tag{4.13}$$

It is noticeable that these solutions can be written in the form of $u_{r,1}^* = r^* f(x^*)$ and $u_{x,1}^* = g(x^*)$ that is consistent with the Von Kármán similarity solution [42] (in which the flow normal to the disk is uniform over planes parallel to the disk). Writing the solution in dimensional form, the radial velocity is:

$$u_{r,1} = \frac{\Omega_o^2 r x(h-x)(6h^2 - 15hx + 5x^2)}{60h^2\nu} \tag{4.14}$$

where it is seen that the radial velocity is a quadratic function of the outer cylinder angular velocity (and consequently Re).

4.3.2 Taylor Couette gap

A steady state solution to the Navier-Stokes equations for infinitely long cylinders is of the form:

$$u_\theta = Ar + \frac{B}{r} \tag{4.15}$$

where A and B are constant:

$$\begin{aligned} A &= \frac{\Omega_o r_o^2 - \Omega_i r_i^2}{r_o^2 - r_i^2}, \\ B &= \frac{(\Omega_i - \Omega_o)(r_i^2\, r_o^2)}{r_o^2 - r_i^2}. \end{aligned} \tag{4.16}$$

For the stationary inner cylinder, A and B simplify to:

$$\begin{aligned} A &= \frac{\Omega_o r_o^2}{r_o^2 - r_i^2}, \\ B &= \frac{\Omega_o (r_i^2\, r_o^2)}{r_i^2 - r_o^2}. \end{aligned} \tag{4.17}$$

This solution shows an almost linear profile of the azimuthal velocity in the gap (Fig 4.2). However, in practice the flow is not purely azimuthal and an Ekman-like circulation is established through the effect of the top and bottom end-walls [43].

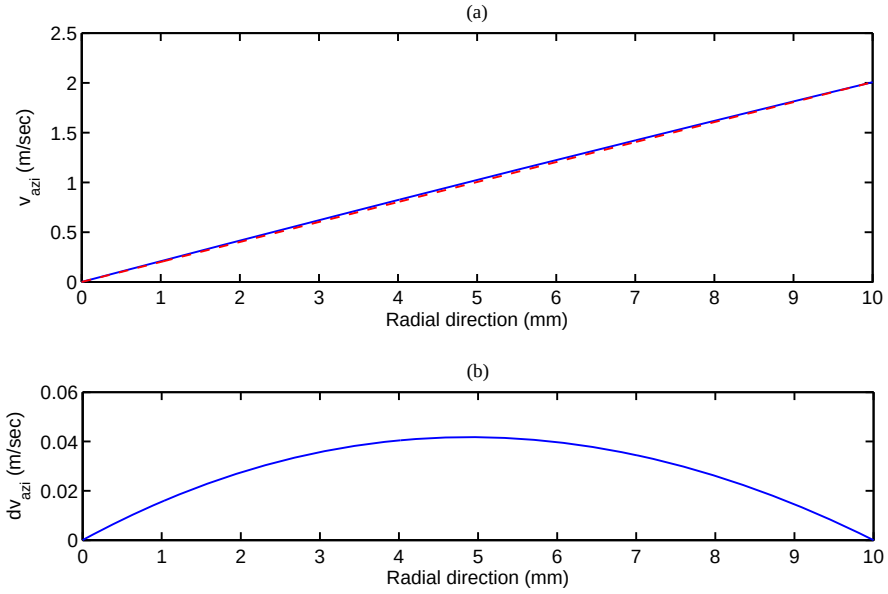

Figure 4.2: Azimuthal velocity in the Taylor Couette gap at $Re = 4000$. **a)** The red dashed-line shows the linear solution whereas the blue line is the exact solution. **b)** The difference between the linear and exact solution.

4.4 Simulation procedure

Several steps are taken to solve the problem numerically. First, the computational domain is generated, and then boundary conditions are specified, and finally the numerical solver is set to compute unknowns of the problem. Each step is briefly explained in the following subsections.

4.4.1 Meshing

In order to obtain an accurate solution, the appropriate mesh has to be generated. A fine mesh with rectangular cells is constructed in the mesh generator program, GAMBIT. Choosing a proper mesh size, which leads to an accurate solution, is an iterative process. One starts with a coarse mesh and solves the problem, and then decreases the size of the mesh and solves it again. This process continues till the difference between the solutions becomes negligible.

4.4.2 Setting boundary condition

To pose the problem correctly, one has to determine the boundary conditions according to the physics of the problem. Obviously, the no-slip boundary condition is proper for the inner and outer cylinder walls. At the interface between water and air, the free-slip boundary condition, which is simply the wall boundary con-

dition with zero shear stress, is chosen. Finally, the axis boundary type is used as the centerline of the axisymmetric geometry.

4.4.3 Numerical method

Finite volume method (FVM) is chosen as the numerical method to evaluate equation (4.1) . Fluent, which is a commercial CFD software is utilized to implement the FVM. In order to reduce numerical diffusion associated with numerical scheme, Third-Order MUSCL (conceived by blending a central differencing scheme and second-order upwind scheme) is used as the highly accurate spatial discretization scheme.

4.5 Results and discussion

4.5.1 Full system

Fig 4.3 shows the vector plot of the velocity field in the Von Kármań region. The primary flow is normal to the plane of the paper (azimuthal direction) whereas the secondary flow is seen in the radial direction. The mechanism generating this boundary-driven secondary flow is straightforward. The centrifugal force is a quadratic function of the azimuthal velocity, which is zero at the inner cylinder end-walls and reaches its maximum value at the outer cylinder end-walls. Near

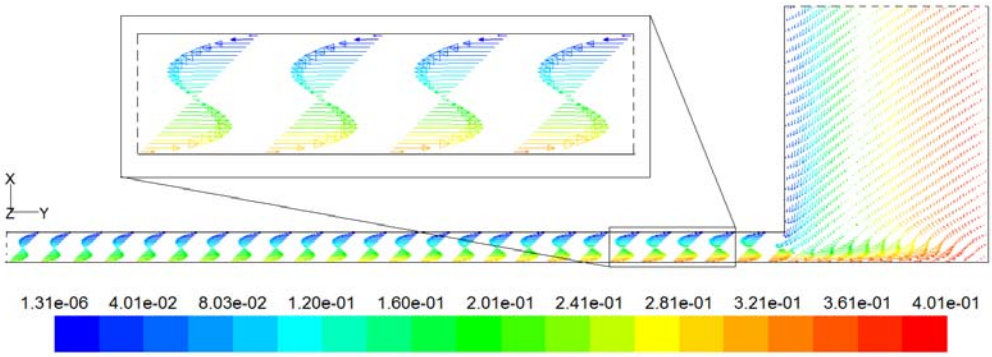

Figure 4.3: Vector plot of velocity profile in Von Kármań region at $Re = 4000$. Colors indicate the azimuthal velocity in meters per second. The inset is the zoom-in of the Von Kármań region close to the Taylor Couette gap.

the outer cylinder end-walls, the outward centrifugal force is larger than the opposite pressure gradient; therefore, an outward motion is observed. The situation is opposite near the inner cylinder end-walls where the flow is pushed inward by the pressure gradient force. This solution is consistent with equation (4.11) in that centrifugal, viscous and pressure gradient forces were the three dominant

forces in the flow. In section 4.7 a comparison is made between the solution obtained from the simulation and the analytical model.

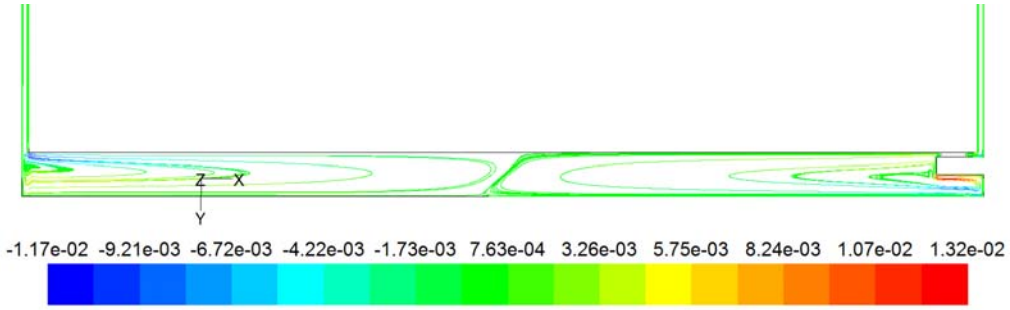

Figure 4.4: Path lines in the Taylor Couette gap at $Re = 4000$. Colors indicate the axial velocity in meters per second. Plot of the set-up is rotated 90 degrees clockwise.

In the Taylor Couette gap, the secondary flow is observed in the form of two meridional circulations which fill the whole height of the gap (shown in Fig 4.4). This secondary flow is caused by the similar reason as the secondary flow in the Von Kármań region. The flow near the outer cylinder end-walls (within the distance of the order of the millimeter from the end-walls) is highly affected by the viscous forces (see Appendix A.1); therefore, there is an imbalance between the pressure gradients and the centrifugal forces in this region which drives the flow in the radial direction. The flow is pushed outward by the imbalanced centrifugal forces and two opposite circulations form. The details of the circulation depend on the top and bottom boundary conditions and the geometrical features of the set-up (i.e. ratio of the radii) [33, 34]. Furthermore, there is a volume of fluid pumped from the Von Kármań region into the Taylor Couette gap which may intensify the circulation. At the top part, this stream of fluid is completely blocked by the metal barrier (depicted by a black rectangle in Fig 4.1).

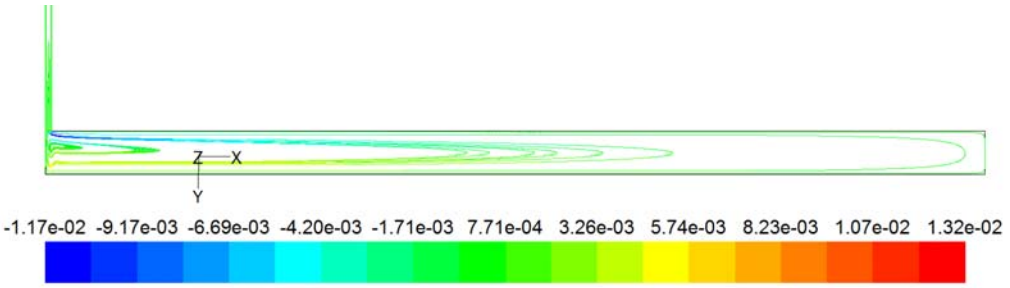

Figure 4.5: Path lines in the Taylor Couette gap at $Re = 4000$. Colors indicate the axial velocity in meters per second. Plot of the set-up is rotated 90 degrees clockwise.

4.5.2 Partially-filled system

The system is filled up to a height of twenty centimeters; therefore, the top end-wall or metal barrier are not included in the geometry, and the flow has an interface with air at the top. Since the free slip boundary condition is assumed for the interface (i.e. no shear stress exists), no boundary layer forms, and thus the Ekman circulation is not induced at the top. This is seen in Fig 4.5 where there is only one circulation occupying the whole height of the gap.

4.6 Dye experiment

A qualitative experiment was implemented to verify the existence of the secondary flow observed in the numerical results. The working fluid was tapped water. Dye particles were added to the flow from the top and the system was remained stationary till the particles settled down on the bottom. Then the outer cylinder was gradually sped up to a desired Reynolds number. The whole process was captured by a CCD camera with frame rate of 10 Hz at resolution of 400x2800 pixels. In order to monitor the height of the colored water, the center column of each image was chosen to be examined. If the light intensity of the column pixels were lower than a threshold, which was defined empirically, they were assigned to one, otherwise to zero. The row where the pixel value changed from zero to

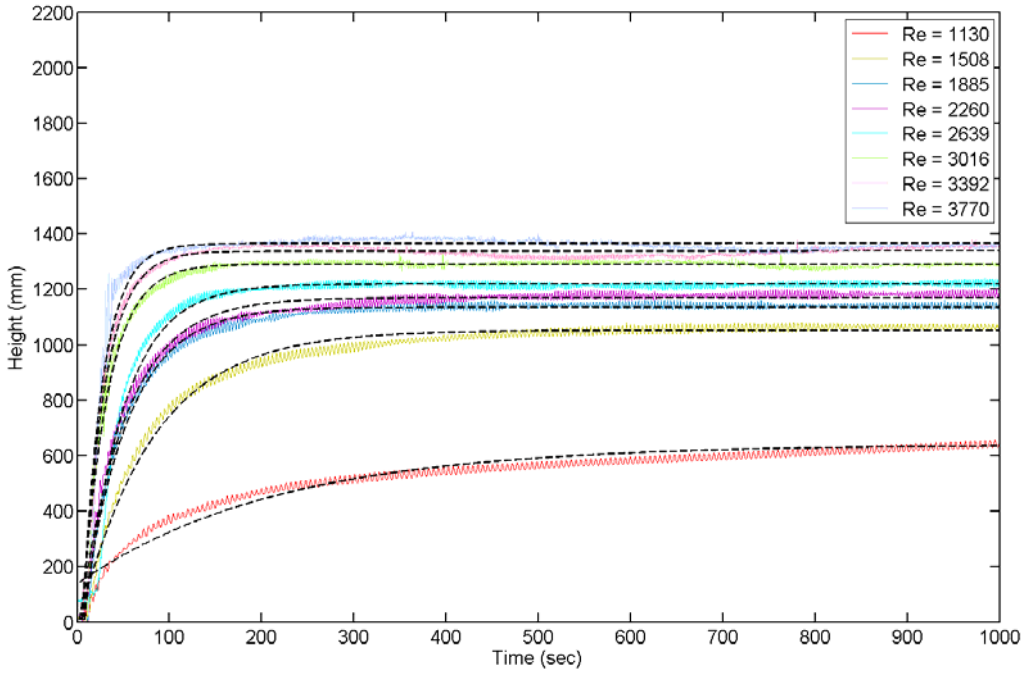

Figure 4.6: The signals indicate the height of the colored water. Black dashed lines are exponential fits defined as, $h(t) = h_\infty(1 - exp(-\frac{t-t_0}{\tau}))$, where h_∞, t_0 and τ are the constants of the fits (given in Table A.1).

one and remained unchanged for the next 30 consecutive rows was identified as the interface between the colored and non-colored water. This procedure was repeated for all images to find a time series of the height of the colored water (Fig 4.6).

The height of the colored water increased with time till it reached a steady point where a sharp interface formed between the colored and non-colored water (Fig 4.7). The upward motion of the colored water is an indicator of the axial velocity in the Taylor Couette gap; moreover, having a sharp interface implies that there is an opposite axial velocity from the top which cancels out the axial flow from the bottom. This is in agreement with the results of the numerical simulation where two large opposite Ekman-cells were observed. As in the numerical simulation, the dye experiment was repeated for the partially-filled system with the water level of twenty centimeters. In this case, the height of the colored water gradually increased till it occupied the whole height of the water which means that there is none or very weak circulation introduced at the top, and therefore, the circulation caused by the bottom plate pushes the color right to the top.

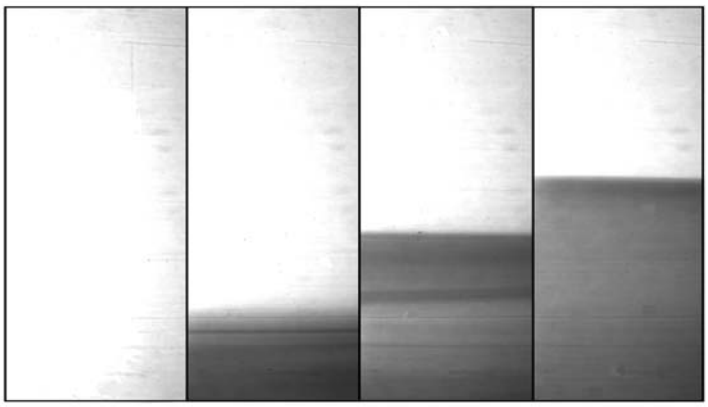

Figure 4.7: Visual evidence of the secondary flow. Four images are taken at time difference $\Delta t = 100$ sec. Height and width of each image illustrate the whole height and a portion of the circumference of the outer cylinder. Black region indicates the water contaminated with dye whereas white region is only water.

4.7 Secondary flow and Reynolds number

The next question is how the secondary flow changes with Reynolds number. By increasing the velocity of the outer cylinder, the velocity of the end-walls attached to the outer cylinder, increases. Consequently, the centrifugal force becomes stronger, and the secondary flow forced by that intensifies. The numerical results show that in the Von Kármań region, the secondary flow increases with the Reynolds number (Fig 4.8) as it was predicted by the analytical model where the radial velocity was found to be a quadratic function of Re (equation (4.14)).

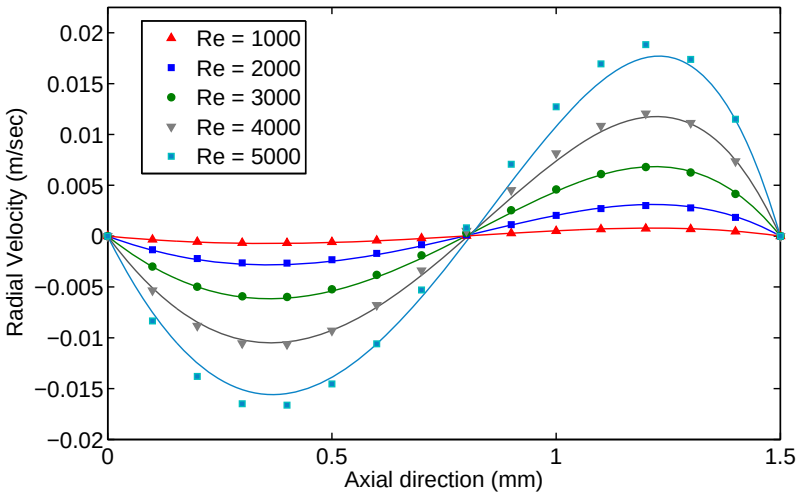

Figure 4.8: Radial velocity in the Von Kármań region for different Reynolds numbers at the distance of r=60 mm from the axis of symmetry. Solid markers and solid lines represent the solutions obtained from the analytical model and simulation along the height of the Von Kármań gap.

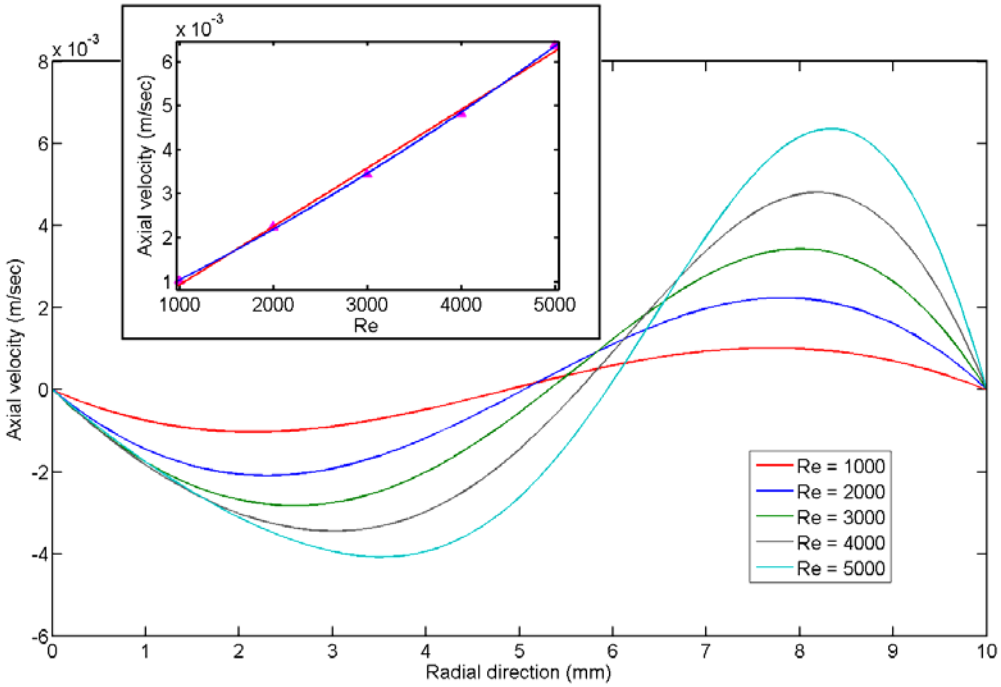

Figure 4.9: Axial velocity vs *Re* in the Taylor Couette gap at the height h=30 mm. Zero and ten in the x-axis are the locations of the inner and outer cylinder walls. Inset, solid markers indicate the maximum amplitude of the axial velocity for the Reynolds numbers, and the red and blue lines are linear and quadratic fits.

Fig 4.9 shows the axial velocity in a cross section of the Taylor Couette gap for different Reynolds numbers where it is seen that the axial velocity increases faster than linearly with Re (Fig 4.9 inset). For the dye experiment, the increase in the axial velocity means that the colored water rises faster and reaches its steady level in less time. This is seen in Fig 4.10 where the time scale of the exponential fits, τ, decreases with Reynolds number. Unfortunately, no function which could properly describe the change of τ with Re and be consistent with the results of the simulation was found.

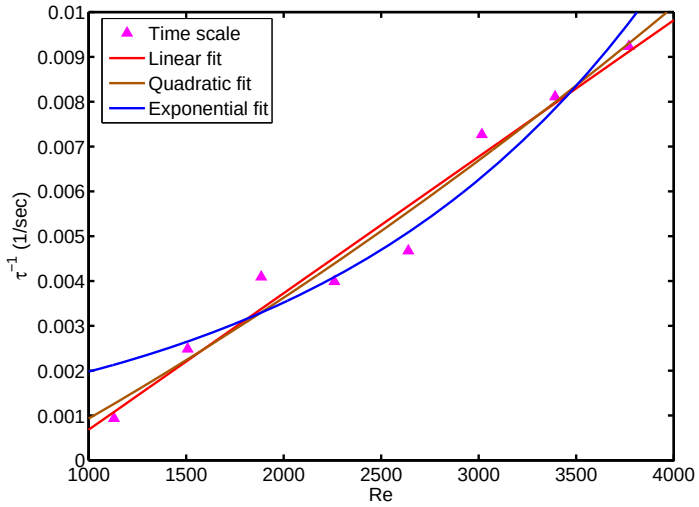

Figure 4.10: The inverse of the time scale of the fitted functions for the height of the colored water.

4.8 Conclusion

Numerical simulation (CFD) has been utilized to gain insight about the laminar flow in the Taylor Couette set-up. The flow was modeled as 2-d axisymmetric and solved using Fluent.

Secondary flow was observed in both the Von Kármań region and the Taylor Couette gap. In the latter, the secondary flow appeared in the form of two opposite circulations occupying the whole height. This secondary flow has its origin with the development of a boundary layer near the end-walls. Existence of the secondary flow was confirmed through a visual experiment, and it was shown that the strength of the secondary flow increases with Reynolds number.

Although the accuracy of the numerical solution has not been tested, useful information about the velocity profile of the laminar flow has been obtained that will be used later on to explain some behaviors of the turbulent patch.

Chapter 5

Lifetime of turbulent patch

5.1 Introduction

In this chapter, the results of the lifetime measurement are presented. The characteristic lifetime of the turbulent patch and its dependency on Reynolds number is studied; moreover, the role of the perturbation type and the boundary condition on the lifetime of the patch is investigated. A comparison is made between the results obtained here and the ones from the previous study [25], and the universal behavior for the lifetime of the turbulent patch is sought. Finally, some other properties of the patch, such as the size and the traveling speed, are examined.

5.2 Patch lifetime

5.2.1 Globally perturbed flow

A general overview of the turbulent patch life cycle is shown in Fig 5.1. First, a global turbulence (Fig 5.1.a), which had been created by the global perturbation, was collapsed to a narrow turbulent ring at the top (Fig 5.1.b). From then on, two different scenarios were observed: either the turbulent ring vanished less than almost 18 seconds and the flow became completely laminar, or it transformed to a tilted shape spot mostly connected to the top lid (Fig 5.1.c). It rotated with the flow for some time and then suddenly disappeared without any precursor.
The lifetime experiment was repeated 100 times for a constant Re, and different decay times were observed. From these, the cumulative probability distribution, which gave the probability of the existence of the patch with time, were calculated. Fig 5.2 shows probability curves for different Reynolds numbers where all curves have a salient feature: the distributions have exponentially decaying tails after the initial time when patch forms. Thus the probability was written as an

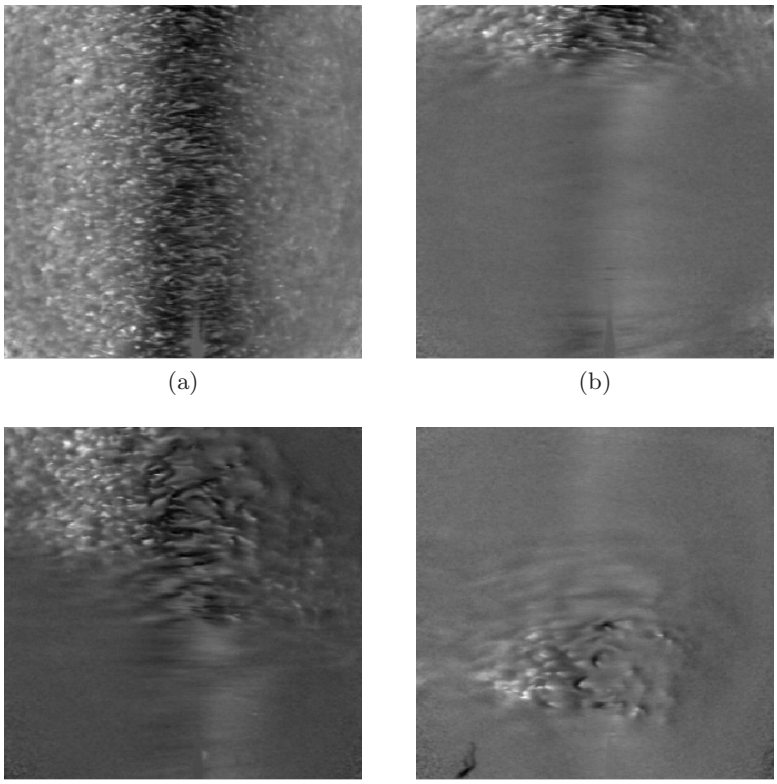

(a) (b)

(c) (d)

Figure 5.1: Life cycle of the turbulent patch in the Taylor Couette flow at $Re = 4530$. Images (a), (b), (c) and (d) are taken at t=2, t=14, t=52 and t=129 seconds, respectively. Image (d) shows the turbulent patch in its last round before it decays.

exponential function of time and Reynolds number, $P(t, Re) \sim exp(-(t)/\tau(Re))$ where τ is the characteristic lifetime calculated by fitting a straight line to the tail of each distribution (see Appendix B.1). This exponential distribution is consistent with the previous study in Taylor Couette flow [25] and has also been observed in pipe and Plane Couette flows [9, 10, 18, 19, 44, 20, 21].

It has to be noted that the observation time in the highest two Reynolds numbers were 20 minutes. After this time, a large portion of particles sedimented on the outer cylinder wall, and hence distinguishing the turbulent patch from laminar flow was less feasible. To check the error introduced by this limitation, the characteristic lifetime, τ, was recalculated for $Re = 4530$ in two different cases where 10 and 40 percent of the points with higher lifetimes were excluded. In the former case, the resulting characteristic lifetime differed by less than 3.5% from the one including all lifetime data points. This difference went up to 10% in the latter case where characteristic lifetime was calculated only by 60% of the data points. In almost 20% of the experiments, the vortex ring disappeared without formation of the patch, and the flow relaminarized. From the dynamical system point of

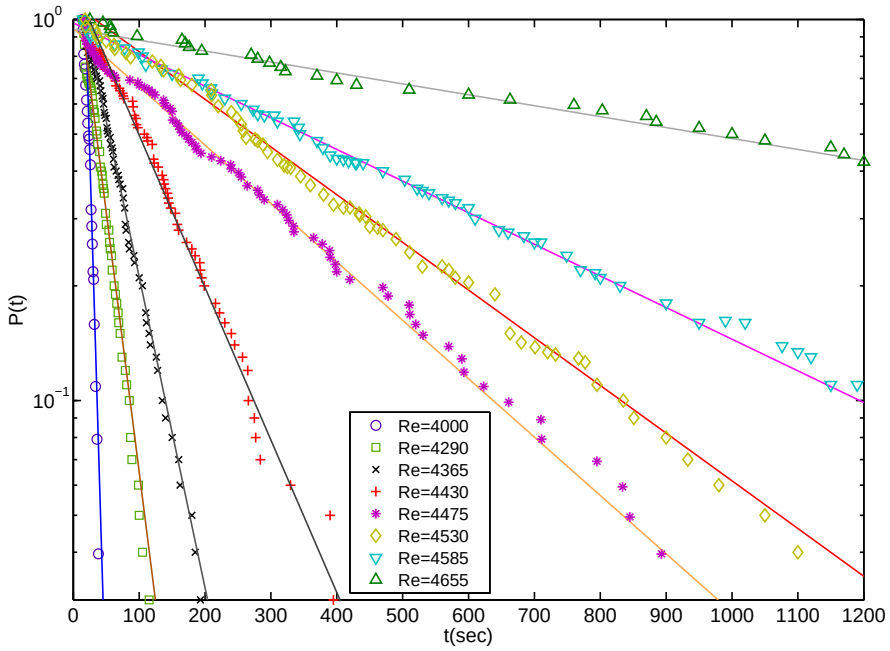

Figure 5.2: Probability of observation of the turbulent patch with time. Lines are exponential fits through the data points which have lifetimes higher than 18 seconds.

view, this can be interpreted as follows: global perturbation force the flow trajectories in the state space to move away from the laminar attractor to a random direction. If they locate near the basin of the chaotic repeller, the turbulent patch forms and the flow behaves chaotic, otherwise the flow becomes laminar again.

It was observed that the characteristic lifetime increased with increasing Reynolds number (see Fig 5.3). From various functions suggested by Hof *et al.* [20] to fit the data (see Appendix B.2), it was found that the super-exponential function,

$$\tau(Re)^{-1} = exp(-exp(aRe + b)) \tag{5.1}$$

with $a = 2.01 \times 10^{-3}$and $b = -7.36$, gave the most accurate fit. Due to the short range of Reynolds number in which the lifetimes have been measured, there are other functions which fit the data better. However, the aim of choosing super-exponential function as the best fit (also suggested by Borrero-Echeverry & Schatz [25]) is to show that the characteristic lifetime increases with Reynolds number faster than exponentially, but it does not diverge to infinity for a finite Re (below the Reynolds number where a global bifurcation occurs).

One question that comes to mind is why the patch formed near the top, remained there for most of its lifetime and quickly decayed after it detached from the top. The only difference between the geometry of the top and the bottom part is the metal barrier attached to the top lid and the resulting gap between the metal

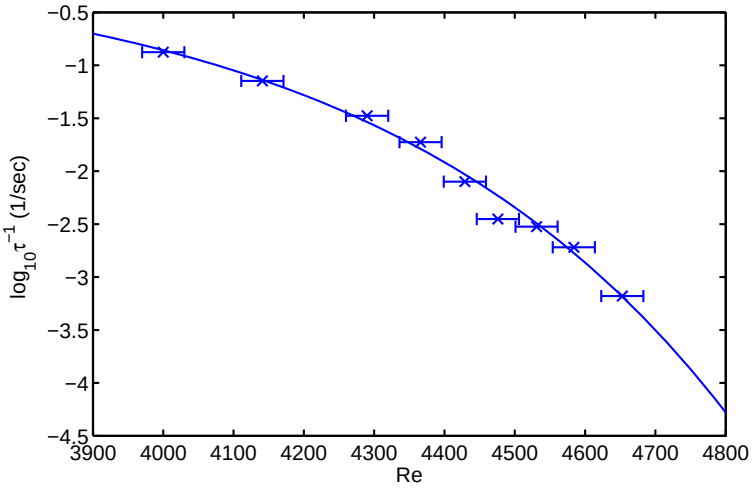

Figure 5.3: Inverse of the characteristic lifetime versus Reynolds number. Horizontal error bars demonstrate the absolute error in Reynolds number based on the experimental limitations, i.e., temperature control and frequency uncertainty.

barrier, the top lid and the outer cylinder wall (shown as region 2 in Fig 5.4.a). To check the effect of this gap, it was filled with a plastic substance (Fig 5.4.b), and the lifetime experiments were repeated. Opposite to the previous situation, the vortex ring shaped near the bottom for all experiments. The patch traveled over the whole height of the Taylor Couette gap, and the characteristic lifetime considerably decreased (see Fig 5.5). There are two probable reasons for such a change in the patch behavior: first, a large circulation and high axial velocity in the filled-gap, predicted by numerical simulation (see Appendix A.2), could

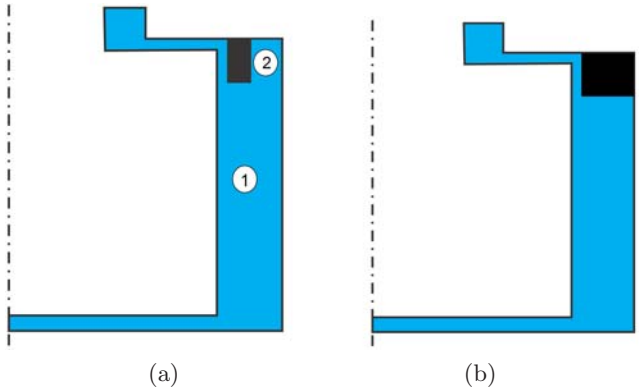

Figure 5.4: Schematic figure of the Taylor Couette system. Blue area is where the flow occurs and the black rectangle is the metal barrier attached to the top lid. **a)** Original system where region 1 is the Taylor Couette gap. **b)** Improved system where region 2 in original system is filled with a plastic substance.

act as a mechanism which fed energy to the turbulent patch and affected its behavior; therefore, by filling the gap, this geometric related high axial velocity was removed. Second, during filling the set-up with water, some air bubbles might be stuck in the gap. Wakes behind the bubbles may have introduced extra disturbances to the flow and consequently affected the behavior of the turbulent patch. From now on the system, in which this gap is filled with the plastic substance, will be named as the "improved system".

5.2.2 Locally perturbed flow

The flow was perturbed by the simultaneous injection and suction of the water through two holes on the inner cylinder. A turbulent patch was formed close to the injection hole and wandered over the whole height of the Taylor Couette gap till it suddenly disappeared. The decay of the turbulent patch had again an exponential distribution (see Appendix B.3) and the characteristic lifetimes were found close to the ones obtained in the globally perturbed flow (Fig 5.5). This means that as long as transition to the intermittent state happens, the type of the perturbation does not significantly affect the lifetime of the turbulent patch.

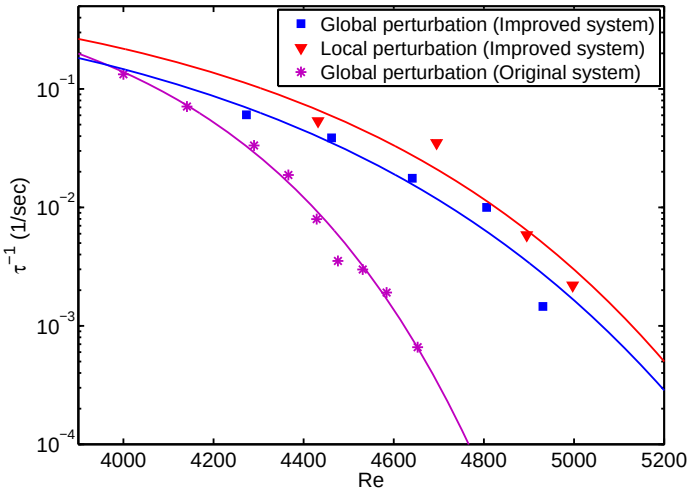

Figure 5.5: The characteristic lifetimes of the turbulent patch for the globally and locally perturbed flow. Solid lines are the fitted super-exponential functions whose constants are $a = 1.2 \times 10^{-3}, 1.34 \times 10^{-3}$ and $b = -4.17, -4.94$ for the globally and locally perturbed flow (both in improved system).

5.3 Scaling laws of patch characteristic lifetime

Fig 5.6 demonstrates the characteristic lifetimes obtained in the current study and the ones reported by Borrero-Echeverry [25]. Obviously at the same Reynolds number, the characteristic lifetime in our system is much higher than those in the Borrero-Echeverry's system. This is not astonishing since the geometrical

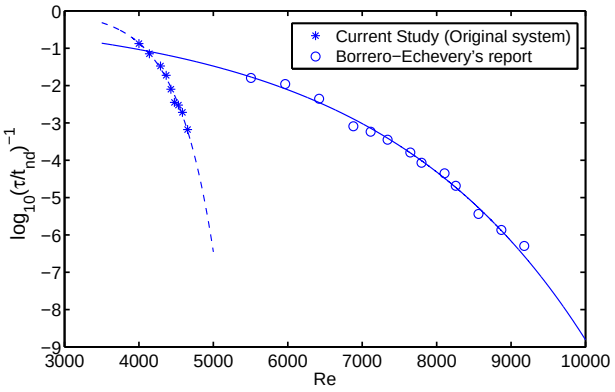

Figure 5.6: The characteristic lifetimes of the turbulent patch have been normalized using advective time units $t_{nd} = d/r_o\Omega_o$. Solid lines are the super-exponential functions fitted through data points.

properties of the systems are different (see Table 5.1); moreover, transition in our Taylor Couette set-up occurs at $Re_{cr} \sim 6000$ while the transition value in the Borrero-Echeverry's system is reported as $Re_{cr} \sim 16000$.

	r_i	r_o	$d = r_o - r_i$	$\eta = r_i/r_o$	$\Gamma = L/d$
Current study	110mm	120mm	10.0mm	0.917	22
Borrero-Echeverry's report	66.38mm	76.20mm	9.82mm	0.871	36

Table 5.1: Geometrical properties of the Taylor Couette set-up

To find a scaling law for the characteristic lifetimes, different scalings based on the geometrical properties and the transition values were tried (see Appendix B.4). It was shown that the characteristic lifetime depends on the aspect ratio Γ [45]; therefore, we chose it as one of the scaling parameters. It is not straightforward what other parameters of the system are influential in determining the characteristic lifetime and have to be used for scaling. The critical Reynolds number (Re_{cr}= 6000 and 16000 for our system and Borrero-Echeverry's system) was chosen as the other scaling parameter which makes the data from two geometries best collapse into one universal series (Fig 5.7). It was shown that the critical Reynolds number is a function of the rotation number which is equal to $R_\Omega = d/r_i$ when the inner cylinder is at rest (see Chapter 2.6). Therefore, by

choosing the transition value as the scaling parameter, we have indirectly considered the rotation number as one of the non-dimensional parameters influencing the lifetime. The characteristic lifetime for the highest Reynolds number in the improved system shows a deviation from the universal trend. Owing to the absence of any data points higher than this value in our system, no conclusion can be made whether this deviation is caused by an experimental error, or the dynamics of the flow may has changed.

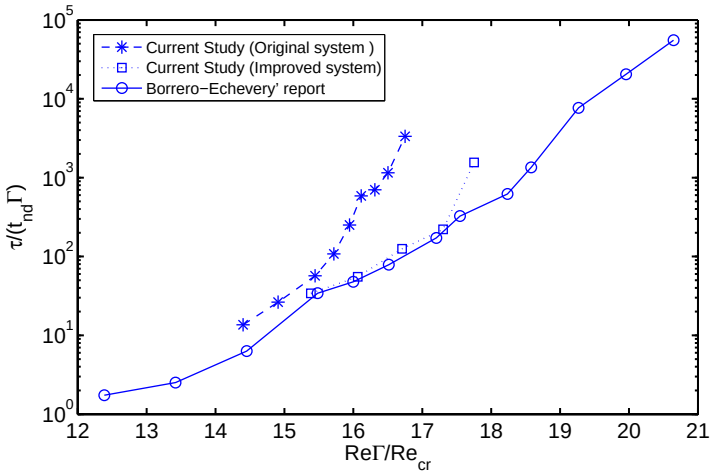

Figure 5.7: Normalized characteristic lifetimes. Reynolds numbers are rescaled by the critical Reynolds number Re_{cr} and the aspect ratio Γ. The characteristic lifetimes are rescaled by the advection time units $t_{nd} = d/r_o\Omega_o$ and the aspect ratio.

5.4 Dependency of patch lifetime on boundary condition

To investigate the dependency of the patch characteristic lifetime on the endwalls, the system was only partially filled with water (i.e. a free surface boundary condition at the top). The lifetime measurement was performed for three different water levels. In order to trigger the transition, the longer duration of the inner cylinder counter-rotation compared to the fully-filled system was required (6 seconds). A similar life cycle and decay distribution to the ones in the completely filled system was observed. It was observed that the characteristic lifetime decreased with lowering the water level in the Taylor Couette gap (Fig 5.8). As mentioned in previous section, the characteristic lifetime is dependent on the aspect ratio; therefore, by changing the water level, the characteristic lifetime changes. Moreover, when the patch touches the air-water interface, possibly some of its turbulent kinetic energy transforms to small surface waves. Hence for the lower water level, there is a higher chance that patch hits the interface and consequently decays in less time. The aspect ratio and critical Reynolds number

were used as the scaling parameters to find a universal series into which the characteristic lifetimes from different heights collapse. Unfortunately, such universal series was not found and thus we infer that the decrease in the characteristic lifetimes may has been caused by the combination of both effects mentioned above.

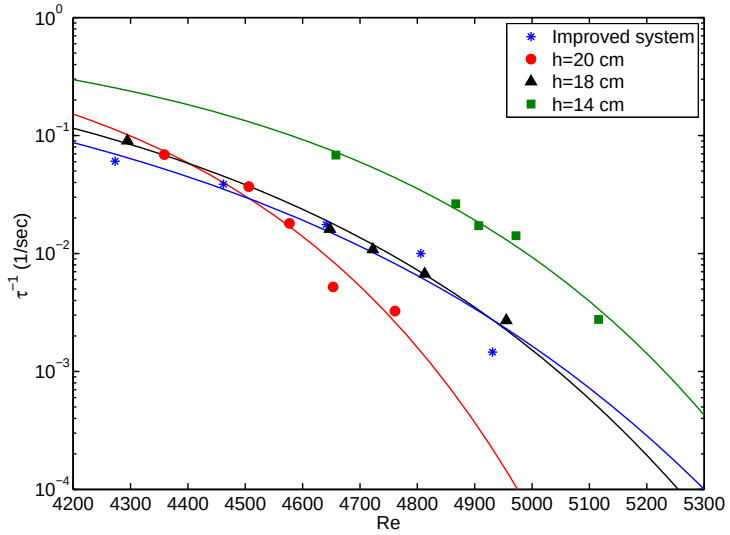

Figure 5.8: The characteristic lifetimes of the turbulent patch for several water level heights "h". Solid lines are the fitted super-exponential functions whose constants are $a = 2.04 \times 10^{-3}, 1.46 \times 10^{-3}, 1.68 \times 10^{-3}$ and $b = -7.96, -5.44, -6.89$ for the water height h= 20, 18 and 14 cm respectively.

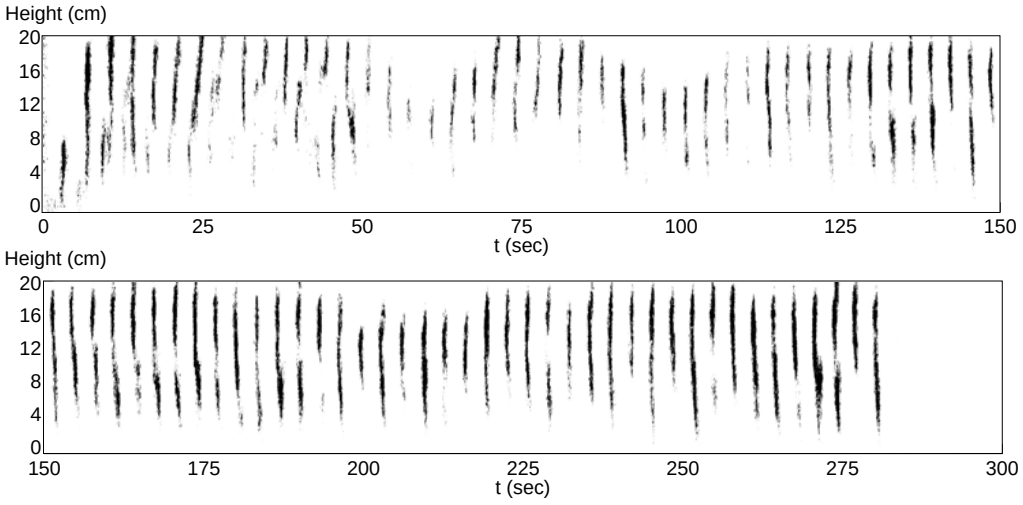

Figure 5.9: Time series of the vertical position of the patch at $Re = 4640$ in the improved system. Black areas represent the turbulent spots whereas white areas indicate the laminar flow.

5.5 Shape and size of turbulent patch

The turbulent patch does not have a constant shape or size. During its life cycle, random behaviors such as contraction, expansion, splitting and merging are observed (Fig 5.9). It is not straightforward what mechanisms in the flow lead to lose or gain of the turbulent kinetic energy of the patch.
It was observed that the average size* of the patch became larger at higher Reynolds numbers (Fig 5.10). It is difficult to relate the increase of the patch size in physical space to the growth of the basin of the chaotic saddle in state space. However, simply speaking by increasing the Reynolds number, more area in the state space is occupied by the basin of the chaotic saddle, and hence more flow trajectories will be located in this basin after the perturbation. Thus more area in the physical space behaves chaotically.

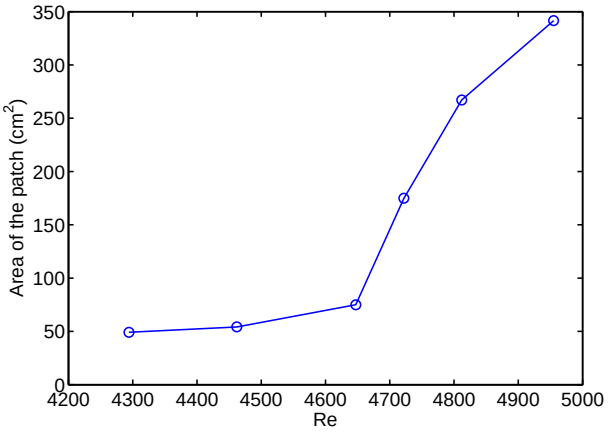

Figure 5.10: Average size of the patch versus Reynolds number. Circles indicate the average size of the patch for each Reynolds number. The turbulent patches were reconstructed from images and their size were calculated (see Appendix C.2).

5.6 Patch and secondary flow

How the secondary flow affects the lifetime of the turbulent patch is still unknown and much more investigation is required to find a quantitative relation between the strength of the secondary flow and the patch lifetime. Nevertheless, the qualitative data reported here suggests an influence of the secondary flow on transition to turbulence; for all of the lifetime experiments (with global perturbation), the turbulent patch was formed near the top or bottom where the secondary flow is strongest (as suggested by the numerical simulation); moreover, it was observed that at the critical Reynolds number, the transition always started from the top

*Average size is defined as the mean of the size of ten consecutive turbulent patches.

or bottom. Hence we infer that the secondary flow introduced by the top and bottom lids have a significant role in the transition to turbulence in our Taylor Couette system.

The last issue discussed in this chapter is the traveling speed of the patch. The angular velocity of the patch is approximated by:

$$U_{patch} \approx (r_i + r_o)\pi f_{patch}, \tag{5.2}$$

where f_{patch} is the average traveling frequency of the patch (see Appendix C.1). It is seen that this angular velocity is close to half of the outer cylinder velocity

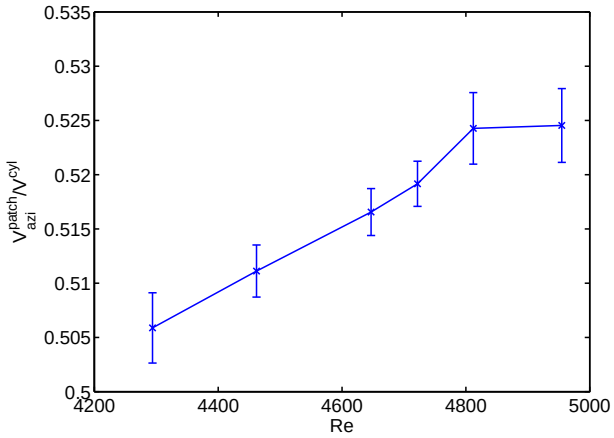

Figure 5.11: Normalized angular velocity of the patch for different Reynolds numbers. Error bars represent the absolute uncertainty in the traveling speed.

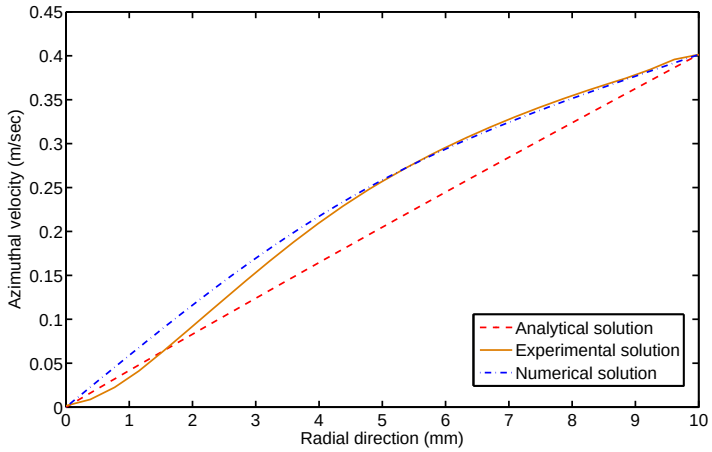

Figure 5.12: Azimuthal velocity profile at the mid height of the Taylor Couette gap (h=110 mm) for $Re = 4000$. Zero and ten in the x-axis are the locations of the inner and outer cylinders. Experimental data was taken from the work of Tokgöz [46].

(Fig 5.11). This is considerably lower than the mean laminar azimuthal velocity which was expected for the patch traveling speed. For instance, at $Re = 4000$ the mean azimuthal velocities obtained from experimental and numerical investigations are 0.229 m/sec and 0.237 m/sec respectively (Fig 5.12), which are almost 14% and 18% higher than the measured patch angular velocity.

Chapter 6

Conclusions and recommendations

This thesis constitutes an investigation of the lifetime of turbulent patches in Taylor Couette flow (with stationary inner cylinder).
Numerical simulation was applied to study the laminar flow with which the turbulent patch coexists. Secondary flow was observed in the form of two meridional circulations filling the whole height of the Taylor Couette gap and its existence was confirmed through a qualitative experiment. It was observed that the secondary flow strengthened with increasing Reynolds number that is in agreement with the experimental measurement of Tokgöz [46].
The lifetime of the turbulent patch has been investigated using flow visualization. The turbulent patch was created by perturbing the laminar flow with two different approaches: global perturbation and local perturbation. It was shown that the characteristic lifetime of the turbulent patch is independent of the perturbation type.
To examine the dependency of the characteristic lifetime on the end-walls, the flow was exposed to air at the top (i.e. the system was partially filled). Similar characteristic lifetimes to the ones in the fully filled system were observed. Furthermore, It was shown that in the partially filled system, the characteristic lifetime depends on the height of the water.
A comparison was made between the characteristic lifetimes obtained here and the ones reported in the previous study [25]. It was shown that although the characteristic lifetime of the intermittent state intensely changes with the geometrical properties of the flow, a universal behavior can be found using the aspect ratio and the critical Reynolds number as scaling parameters.
It was shown that for all lifetime experiments, the decay of the turbulent patch has an exponential distribution. This suggests that the chaotic saddle model is

the correct model for this flow independent of the perturbation type or boundary condition at end-walls.

Finally, some other properties of the turbulent patch, like shape, size and traveling speed, were examined. It was observed that the turbulent patch does not have a constant size or shape in its life cycle. Furthermore, it was shown that the average size and the traveling speed of the turbulent patch increase with increasing the Reynolds number.

There are several open questions remained as subjects for further investigation. In the range of Reynolds numbers studied here and in the previous study [25], it was shown that the characteristic lifetime increases with Reynolds number faster than exponentially. It is still unknown whether the characteristic lifetime remains bounded specially near the critical Reynolds number which suggests that the chaotic transient model is applicable for all Reynolds numbers (below the Reynolds number where a global bifurcation occurs), or it tends to infinity and the turbulence sustains. Moreover, critical amplitude of the global or local perturbation to create the turbulent patch has not determined. Furthermore, the role of the end-walls, which introduce a secondary flow and limit the motion of the turbulent patch, on the lifetime is not completely understood. Finally, the inner structure of the turbulent patch, which could provide useful information about the interaction mechanisms between the patch and the laminar flow, is not resolved.

Bibliography

[1] B. Eckhardt, H. Faisst, A. Schmiegel & T.M. Schneider. Dynamical systems and the transition to turbulence in linearly stable shear flows. *Phys. Trans. R. Soc*, 8:1297–1315, Apr 2008. [cited at p. 1, 2, 5, 18]

[2] O. Reynolds. An experimental investigation of the circumstances which determine whether the motion of water in parallel channels shall be direct or sinuous and of the law of resistance in parallel channel. *Phil. Trans. R. Soc*, 174. [cited at p. 1]

[3] R.R Kerswell. Recent progress in understanding the transition to turbulence in a pipe. *Nonlinearity*, 18(6):R17, 2005. [cited at p. 1]

[4] P. Holmes, J. L. Lumley & G. Berkooz. *Turbulence, coherent structures, dynamical systems and symmetry*. Cambridge University Press, 1996. [cited at p. 1, 2]

[5] P. J. Schmid & D. S.Henningson. *Stability and transition of shear flows*. New York, NY: Springer, 1999. [cited at p. 1]

[6] U. Brosa. Turbulence without strange attractor. *Statistical Physics*, 55, 1989. [cited at p. 1]

[7] J. Guckenheimer. Strange attractors in fluids. *Rev. Fluid Mech*, 18:15–31, 1986. [cited at p. 2]

[8] J. Guckenheimer & P. Holmes. *Nonlinear Oscillations, Dynamical Systems, and Bifurcation of Vector Fields*. Springer-Verlag, 1983. [cited at p. 2]

[9] J. Peixinho & T. Mullin. Decay of turbulence in pipe flow. *Phys. Rev. Lett*, 96(9), 2006. [cited at p. 3, 4, 5, 18, 35]

[10] S. Bottin & H. Chaté. Statistical analysis of the transition to turbulence in plane Couette flow. *Eur. Phys*, 6:143–155, June 1998. [cited at p. 3, 35]

[11] H. Faisst& B. Eckhardt. Sensitive dependence on initial conditions in transition to turbulence in pipe. *Fluid Mech*, Jan 2004. [cited at p. 3]

[12] L. P. Kadanoff & C. Tang. Escape from strange repellers. *Phys. Rev. A*, 81(4):1276–1279, 1984. [cited at p. 3]

[13] H. Kantz & P. Grassberger. Repellers, semi-attractors and long-lived chaotic transients. *Physica 17D*, pages 75–86, 1985. [cited at p. 3]

[14] B. Eckhardt, T. M. Schneider, B. Hof & J. Westerweel. Turbulence transition in pipe flow. *Annu. Rev. Fluid Mech*, 39, 2007. [cited at p. 3]

[15] S. K. Robinson. Coherent motions in the turbulent boundary layer. *Rev. Fluid Mech*, 23:601–39, 1991. [cited at p. 4]

[16] B. Hof, C. W. H. Van Doorne, J. Westerweel, F. T. M. Nieuwstadt, H. Faisst, B. Eckhardt, H. Wedin, R. R. Kerswell & F. Waleffe. Experimental observation of nonlinear traveling waves in turbulent pipe flow. *Science*, 305:1594, 2004. [cited at p. 4]

[17] F. Daviaud, J. Hegseth & P. Bergé . Subcritical transition to turbulence in plane Couette flow. *Phys. Rev. Lett*, 69(17):2511–2514, Oct 1992. [cited at p. 5]

[18] A. P. Willis & R. R. Kerswell. Critical behavior in the relaminarization of localized turbulence in pipe flow. *Phys. Rev. Lett*, 98(1), January 2007. [cited at p. 5, 35]

[19] B. Hof, J. Westerweel, T. M. Schneider & B. Eckhardt. Finite lifetime of turbulence in shear flows. *Nature*, 443(7107):59–62, 2006. [cited at p. 5, 6, 7, 18, 35]

[20] B. Hof, A. de Lozar, D.J. Kuik & J. Westerweel. Repeller or attractor? selecting the dynamical model for the onset of turbulence in pipe flow. *Phys. Rev. Lett*, 101(214501), 2008. [cited at p. 5, 35, 36]

[21] P. Manneville. Understanding the sub-critical transition to turbulence in wall flows. *PRAMANA, Indian Academy of Sciences*, 70(6), 2008. [cited at p. 5, 35]

[22] T. M. Schneider& B. Eckhardt. Turbulence transition and the edge of chaos in pipe flow. *Phys. Rev. Lett*, 2007. [cited at p. 5]

[23] T. Shinbrot, C. Grebogi, J. A. Yorke & E. Ott. Using small perturbations to control chaos. *Nature*, 363:411–417, 1993. [cited at p. 5]

[24] J. D. Skufca, J. A. Yorke & Bruno Eckhardt. Edge of chaos in a parallel shear flow. *Phys. Rev. Lett*, 96, 2006. [cited at p. 6]

[25] D. Borrero-Echeverry & M. F. Schatz. Transient turbulence in Taylor-Couette flow. *Phys. Rev. E*, 81(2):025301, Feb 2010. [cited at p. 7, 17, 18, 34, 35, 36, 39, 45, 46]

[26] R. Tagg. The Couette-Taylor problem. *Non linear Science*, 4, 1994. [cited at p. 9]

[27] C. D. Andereck, S. S. Liu & H. L. Swinney. Flow regimes in circular Couette system with independently rotating cylinder. *Fluid Mech*, 164:155–183, 1985. [cited at p. 9, 10, 11, 17]

[28] D. Coles. Transition in circular Couette flow. *Fluid Mech*, 21:385–425, 1965. [cited at p. 9, 11]

[29] B. Dubrulle, O. Dauchot, F. Daviaud, P. Y. Longaretti, D. Richard & J. P. Zahn. Stability and turbulent transport in Taylor-Couette flow from analysis of experimental data. *Physics of Fluids*, 17(9), September 2005. [cited at p. 10, 11, 13, 14, 15]

[30] P. Y. Longaretti & O. Dauchot. Subcritical turbulent transition in rotating and curved shear flows. *Fluid Mechanics and Its Applications*, September 2005. [cited at p. 12]

[31] P. Y Longaretti. On the phenomenology of hydrodynamic shear turbulence. *The Astrophysical Journal*, 576(1):587, 2002. [cited at p. 12]

[32] P. K. Kundu & I. M. Cohen. *Fluid Mechanics*. ELSEVIER, 4st, edition, 2008. [cited at p. 13]

[33] D. Richard. *Instabilités hydrodynamiques dans les écoulements en rotation différentielle*. PhD thesis, Université de paris, 2001. [cited at p. 14, 15, 29]

[34] G. Wendt. Turbulente Strömung Zwischen Zwei Rotierenden Konaxialen Zylindern. *Ing.-Arch*, 4:577, 1933. [cited at p. 14, 15, 29]

[35] D. K. Lezius & J. P. Johnston. Roll-cell instabilities in rotating laminar and turbulent channel flows. *Fluid Mech*, 77, 1976. [cited at p. 14]

[36] A. Esser & S. Grossmann. Analytic expression for Taylor Couette stability boundary. *Phys. Fluids*, 8:1814–1819, 1996. [cited at p. 14]

[37] G. I. Taylor. Fluid friction between rotating cylinders. *Proc. R. Soc. London, Ser.A*, 157, 1936. [cited at p. 15]

[38] A. N. Tillmark & P. H. Alfredsson. Experiments on rotating plane Couette flow. *In Advances in Turbulence VI*, pages 391–394, 1996. [cited at p. 15]

[39] N. Abcha, N. Latrache, F. Dumouchel & I. Mutabazi. Qualitative relation between reflected light intensity by Kalliroscope flakes and velocity field in the Couette Taylor flow system. *Exp Fluids*, 45(1):85–94, February 2008. [cited at p. 17]

[40] Ö. Savas. On flow visualization using reflective flakes. *Fluid Mech*, 152:235–248, 1985. [cited at p. 17]

[41] R. Delfos. Theoretical model for the flow between two finite rotating discs, "Private Communication", 2011. Laboratory for Aero & Hydrodynamics in Delft University of Technology. [cited at p. 25]

[42] Von Kármán. Über laminare und turbulente reibung. *Phys. Rev. E*, 1(4):233–5, 1921. [cited at p. 26]

[43] M. J. Burin, H. Ji, E. Schartman, R. Cutler, P. Heitzenroeder, W. Liu, L. Morris & S. Raftopolous. Reduction of Ekman circulation within Taylor-Couette flow. *Experiments in Fluids*, 40:962–966, 2006. [cited at p. 26]

[44] M. Lagha & P. Manneville. Modeling transitional plane Couette flow. *Eur. Phys. J. B*, 58:433–447, 2007. [cited at p. 35]

[45] D. B. Echeverry & M. F. Schatz. Transient Turbulence in Taylor-Couette Flow. Presentation at 16th Couette-Taylor Workshop at Princeton University, 2009. [cited at p. 39]

[46] S. Tokgöz. Investigation of velocity profile in Taylor Couette flow with stationary inner cylinder using Tomo-PIV, "Private Communication", 2011. Laboratory for Aero & Hydrodynamics in Delft University of Technology. [cited at p. 43, 45]

Appendix A

Results from numerical simulation

A.1 Boundary layer approximation in Taylor Couette gap

Assuming steady axisymmetric incompressible flow, momentum equation in radial direction is as follow:

$$u_r \frac{\partial u_r}{\partial r} - \frac{u_\theta^2}{r} + u_x \frac{\partial u_r}{\partial x} = -\frac{\partial p}{\rho \partial r} + \nu \frac{\partial^2 u_r}{\partial x^2} + other\ 2^{nd}\ derivatives \tag{A.1}$$

The basic idea is that variations across the boundary layer are much faster than variations along the layer, that is

$$\frac{\partial^2}{\partial r^2} << \frac{\partial^2}{\partial x^2} \tag{A.2}$$

So we can neglect the other second derivative terms in equation (A.1). Considering r_o and $r_o\Omega_o$ as the characteristic length and velocity of the flow, a measure of the centrifugal term in equation (A.1) is:

$$\frac{u_\theta^2}{r} \sim \frac{r_o^2 \Omega_o^2}{r_o} \tag{A.3}$$

where $\sim$ is to be interpreted as "of order". A measure of the viscous term in equation (A.1) is:

$$\nu \frac{\partial^2 u_r}{\partial x^2} \sim \nu \frac{r_o \Omega_o}{\delta^2} \tag{A.4}$$

where δ is the thickness of the layer in which viscose forces are influential. The magnitude of δ can now be estimated by noting that the centrifugal and viscous terms should be of the same order within the boundary layer, if viscous terms are to be important. Equating equations (A.3) and (A.4), we obtain:

$$\delta \sim \sqrt{\frac{\nu}{\Omega_o}} \tag{A.5}$$

Therefore, with the values for ν and Ω_o given in chapter 4, δ can be approximated as of the order of a millimeter.

A.2 Axial velocity in Taylor Couette system

Figure A1-A3 show the numerical simulation results for the original, improved and partially-filled systems respectively.

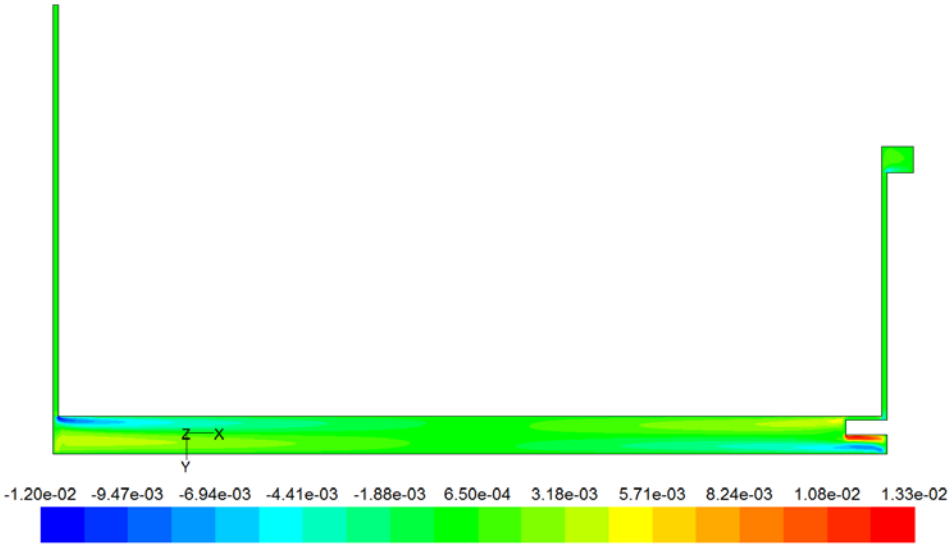

Figure A.1: Axial velocity in Taylor Couette system at $Re = 4000$. Colors indicate the magnitude of axial velocity in meters per second. Plot of the set-up is rotated 90 degrees clockwise.

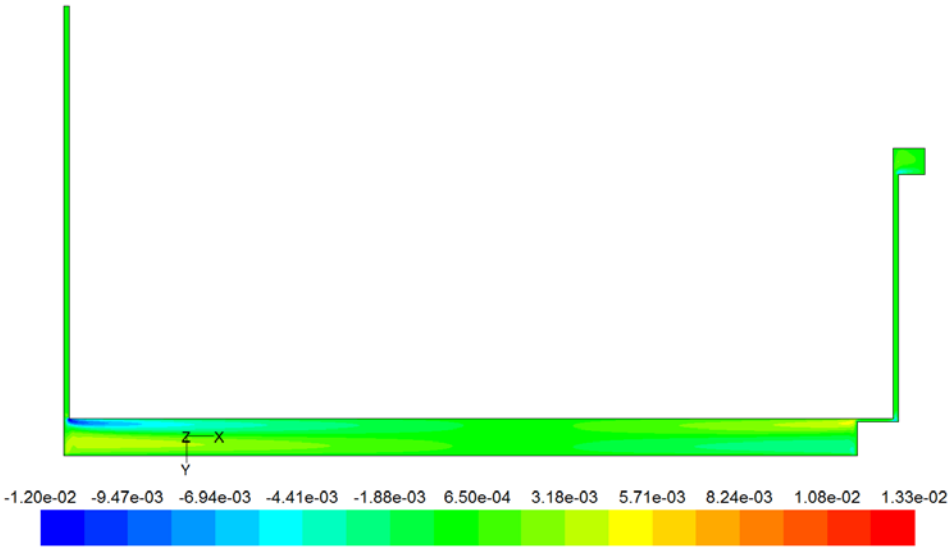

Figure A.2: Axial velocity in improved system at $Re = 4000$. Colors indicate the magnitude of axial velocity in meters per second. Plot of the set-up is rotated 90 degrees clockwise.

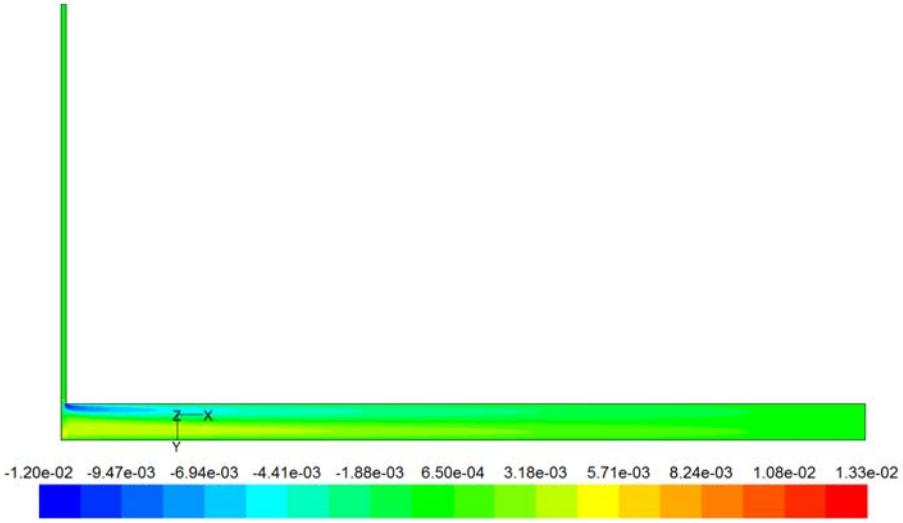

Figure A.3: Axial velocity in partially-filled system at $Re = 4000$. Colors indicate the magnitude of axial velocity in meters per seconds. Plot of the set-up is rotated 90 degrees clockwise.

A.3 Height of colored water

Table A.1 shows the constants of the exponential functions fitted through the data points in Fig 4.6.

Re	h_∞ (mm)	t_0 (sec)	τ (sec)
$1,130$	641.0	-51.52	214.2
$1,508$	$1,053$	1.371	80.60
$1,885$	$1,137$	4.886	48.86
$2,260$	$1,170$	2.340	50.16
$2,639$	$1,220$	7.426	42.80
$3,016$	$1,292$	5.020	27.52
$3,392$	$1,339$	5.148	24.66
$3,770$	$1,365$	5.836	21.66

Table A.1: Constants of the exponential fits.

Appendix B

Lifetime measurement

B.1 Measured characteristic lifetimes

Table B.1-B.4 show the measured characteristic lifetimes τ as a function of outer cylinder Reynolds number for different geometries, boundary conditions and perturbations of the Taylor Couette flow. σ_τ is the error in the characteristic lifetimes which is calculated based on 95% condfidence inetrvals for the linear fitting parameter.

Re	τ (sec)	σ_τ (sec)	Re	τ (sec)	σ_τ (sec)
4,000	7.53×10^0	$\pm 4.97 \times 10^{-1}$	4,475	2.83×10^2	$\pm 9.39 \times 10^0$
4,290	3.18×10^1	$\pm 9.39 \times 10^{-1}$	4,530	3.47×10^2	$\pm 1.33 \times 10^1$
4,365	5.32×10^1	$\pm 1.35 \times 10^0$	4,585	5.23×10^2	$\pm 1.14 \times 10^1$
4,430	1.25×10^2	$\pm 3.41 \times 10^0$	4,655	1.51×10^3	$\pm 4.33 \times 10^1$

Table B.1: Measured characteristic lifetimes τ in the original system.

H=18 cm			H=20 cm		
Re	τ (sec)	σ_τ (sec)	Re	τ (sec)	σ_τ (sec)
4,294	1.10×10^1	$\pm 7.33 \times 10^{-1}$	4,358	1.14×10^1	$\pm 1.40 \times 10^0$
4,462	1.48×10^1	$\pm 6.20 \times 10^{-1}$	4,506	2.71×10^1	$\pm 0.97 \times 10^{-1}$
4,647	6.20×10^1	$\pm 2.26 \times 10^0$	4,577	5.56×10^1	$\pm 2.51 \times 10^0$
4,722	9.23×10^1	$\pm 4.15 \times 10^0$	4,653	1.92×10^2	$\pm 7.51 \times 10^0$
4,812	1.48×10^2	$\pm 5.43 \times 10^0$	4,761	3.07×10^2	$\pm 1.64 \times 10^1$
4,955	3.69×10^2	$\pm 1.36 \times 10^1$			

H=14 cm		
Re	τ (sec)	σ_τ (sec)
$4,658$	1.46×10^1	$\pm 8.30 \times 10^{-1}$
$4,867$	3.79×10^1	$\pm 1.65 \times 10^0$
$4,907$	5.81×10^1	$\pm 3.375 \times 10^0$
$4,972$	7.06×10^1	$\pm 1.99 \times 10^0$
$5,116$	3.62×10^2	$\pm 1.08 \times 10^1$

Table B.2: Measured characteristic lifetimes τ in the partially-filled system. H represents the height of the water in the Taylor Couette gap.

Re	τ (sec)	σ_τ (sec)
$4,273$	1.65×10^1	$\pm 1.44 \times 10^0$
$4,462$	2.58×10^1	$\pm 1.54 \times 10^0$
$4,641$	5.67×10^1	$\pm 2.75 \times 10^0$
$4,806$	1.00×10^2	$\pm 1.30 \times 10^1$
$4,931$	6.85×10^2	$\pm 2.18 \times 10^1$

Table B.3: Measured characteristic lifetimes τ in the improved system with global perturbation.

Re	τ (sec)	σ_τ (sec)
$4,432$	1.86×10^1	$\pm 1.11 \times 10^0$
$4,695$	2.85×10^1	$\pm 7.39 \times 10^{-1}$
$4,895$	1.71×10^2	$\pm 4.92 \times 10^0$
$4,997$	4.55×10^2	$\pm 1.67 \times 10^1$

Table B.4: Measured characteristic lifetimes τ in the improved system with local perturbation.

B.2 Functions fitted through characteristic lifetimes

Fit parameters of characteristic lifetime as a function of Re in the improved system (where flow was perturbed globally).

Fit	Parameter	Value	95%Confidence Interval	R-squared
$\tau = exp(exp(c_1 Re + c_2))$	c_1	2.01×10^{-3}	$(1.84 \times 10^{-3}, 2.18 \times 10^{-3})$	0.991
	c_2	-7.36×10^{0}	$(-8.19 \times 10^{0}, -6.613 \times 10^{0})$	
$\tau = exp(c_3 Re + c_4)$	c_3	3.54×10^{-3}	$(2.88 \times 10^{-3}, 4.20 \times 10^{-3})$	0.958
	c_4	-1.35×10^{1}	$(-1.64 \times 10^{1}, -1.06 \times 10^{1})$	
$\tau = exp((Re/c_5)^{c_6})$	c_5	4.07×10^{3}	$(4.02 \times 10^{3}, 4.12 \times 10^{3})$	0.988
	c_6	8.74×10^{0}	$(7.73 \times 10^{0}, 9.75 \times 10^{0})$	
$\tau = c_7/(Re_{c,1} - Re)^{c_8}$	c_7	1.96×10^{-6}	$(-2.31 \times 10^{-2}, 2.31 \times 10^{-2})$	0.102
	c_8	-2.26×10^{0}	$(-1.27 \times 10^{-3}, 1.26 \times 10^{3})$	
	$Re_{c,1}$	7.48×10^{0}	$(-2.43 \times 10^{6}, 2.42 \times 10^{6})$	
$\tau = exp(c_9/(Re_{c,2} - Re)^{c_{10}})$	c_9	2.24×10^{-7}	$(-5.4 \times 10^{-4}, 5.4 \times 10^{-4})$	0.423
	c_{10}	-1.93×10^{0}	$(-2.62 \times 10^{2}, 2.58 \times 10^{2})$	
	$Re_{c,2}$	1.54×10^{1}	$(-5.88 \times 10^{5}, 5.88 \times 10^{5})$	

Table B.5: Fit parameters for different functions.

B.3 Lifetime distribution of turbulent patch

Fig B.1-B.4 demonstrate the lifetime distribution of the turbulent patch for locally perturbed flow and partially-filled system.

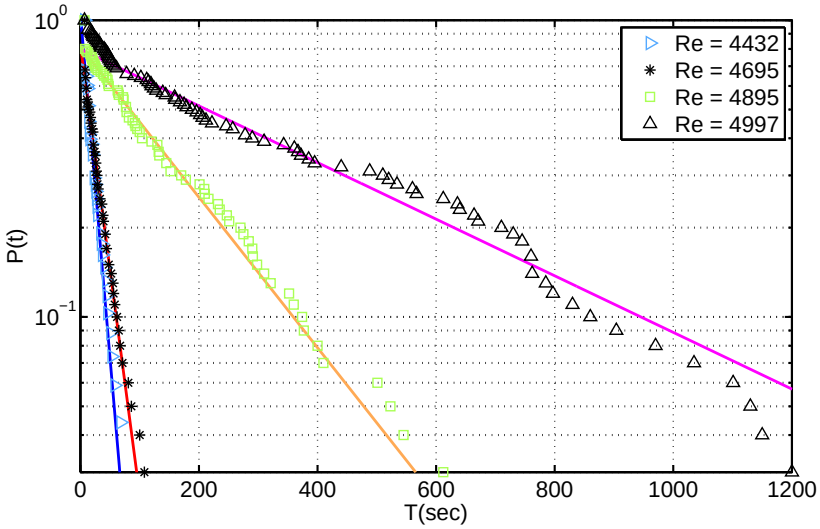

Figure B.1: Probability of observation of turbulent patch with time. Each point indicates the probability of the existence of the patch at a certain time. Lines are exponential fit through the data points which had lifetimes higher than 8 seconds.

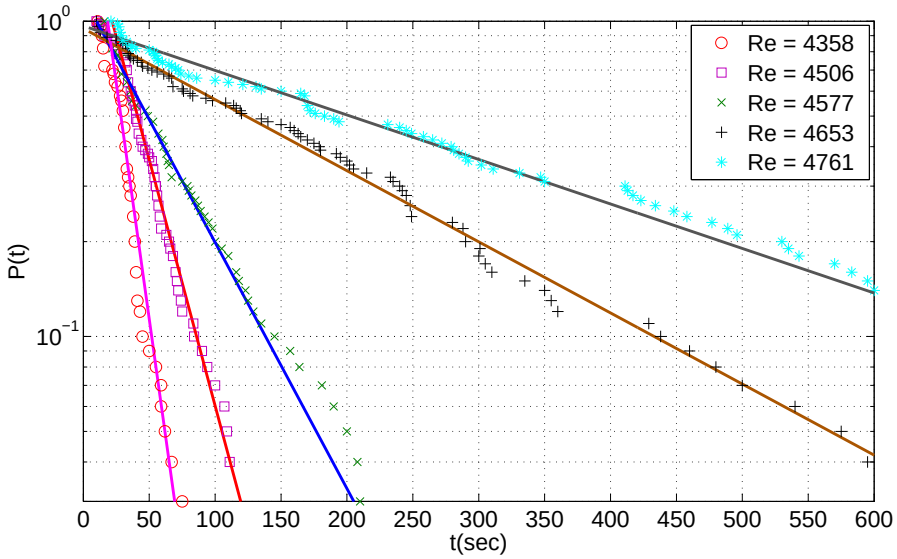

Figure B.2: Probability of observation of turbulent patch with time in partially filled system with water level of 20 cm. Each point indicates the probability of the existence of the patch at a certain time. Lines are exponential fit through the data points which had lifetimes higher than 18 seconds.

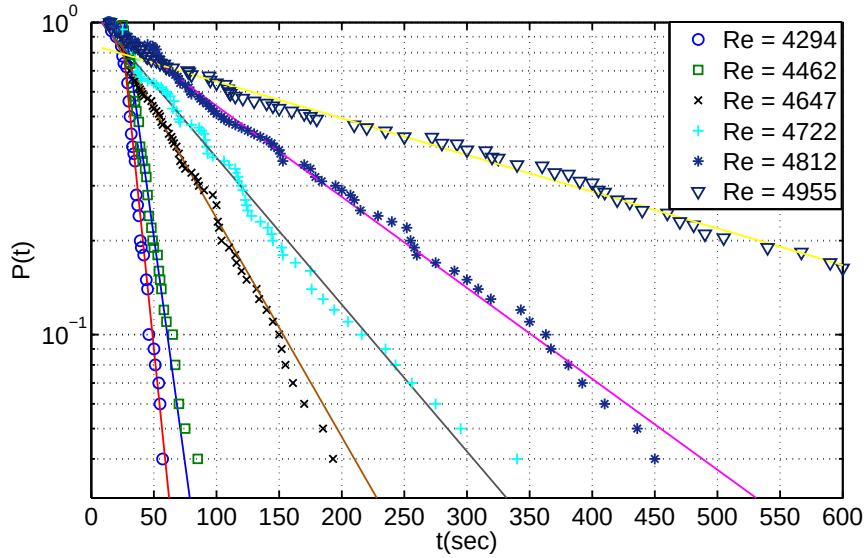

Figure B.3: Probability of observation of turbulent patch with time in partially filled system with water level of 18 cm. Each point indicates the probability of the existence of the patch at a certain time. Lines are exponential fit through the data points which had lifetimes higher than 18 seconds.

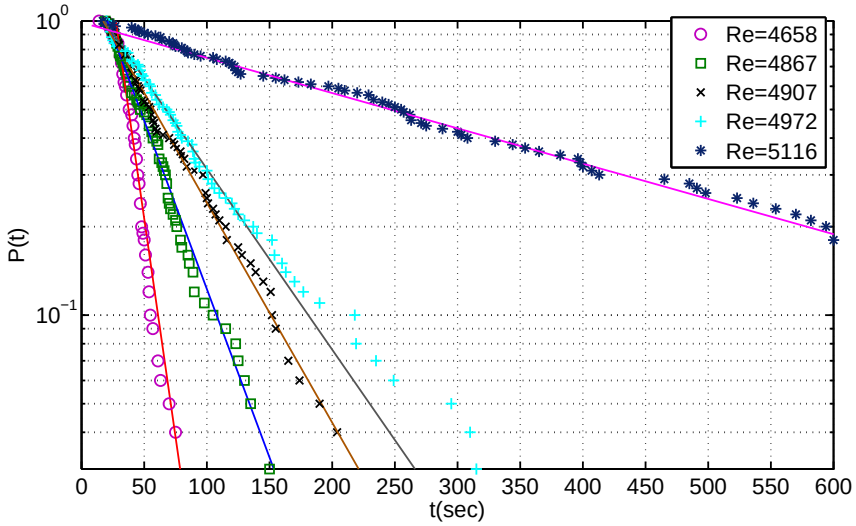

Figure B.4: Probability of observation of turbulent patch with time in partially filled system with water level of 14 cm. Each point indicates the probability of the existence of the patch at a certain time. Lines are exponential fit through the data points which had lifetimes higher than 18 seconds.

B.4 Scaling laws of patch characteristic lifetime

Fig B.5 and Fig B.6 show scaling of the characteristic lifetime with different parameters of the flow.

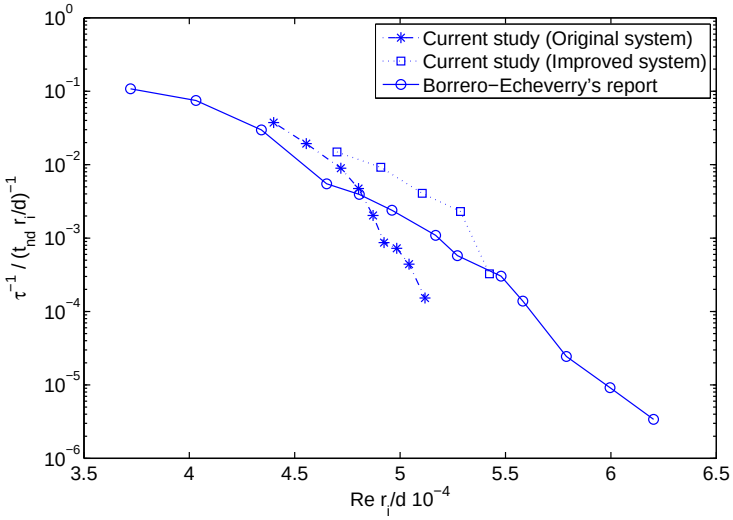

Figure B.5: Normalized characteristic lifetimes. Reynolds numbers are rescaled by the inner cylinder radius to the gap ratio r_i/d. The characteristic lifetimes are rescaled by the advective time unit t_{nd} and r_i/d.

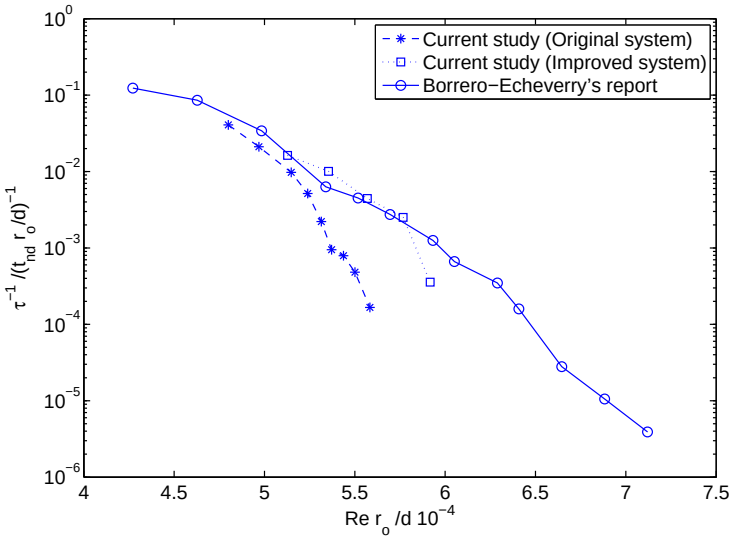

Figure B.6: Normalized characteristic lifetimes. Reynolds numbers are rescaled by the outer cylinder radius to the gap ratio r_o/d. The characteristic lifetimes are rescaled by the advective time unit t_{nd} and r_o/d

Appendix C

Average size and traveling frequency of turbulent patch

C.1 Average traveling frequency of patch

After obtaining the time series of the vertical position of the patch (Fig 5.9), the time to capture 25 consecutive patches is computed. Having this time and dividing it by 25, the average frequency of the patch f_{patch} is obtained. Fig C.1 shows the traveling frequency of the patch for different Reynolds numbers.

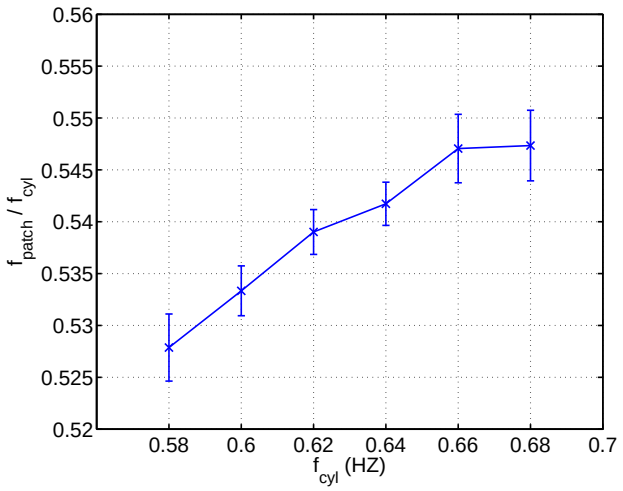

Figure C.1: Average rotational frequency of the turbulent patch normalized by the outer cylinder frequency. The error bars represent the standard error of ten measurements.

C.2 Average size of turbulent patch

Using the average azimuthal velocity of the patch, U_{patch} (obtained from equation 5.2), the distance that patch travels in each image is estimated by:

$$X \approx \frac{U_{patch}}{f_{cam}} \tag{C.1}$$

where f_{cam} is the camera recording frequency. By cutting out this width of each image and attaching it to the one of next image, the reconstructed image of the patch was obtained without losing or gaining of its area (Fig C.2). Each pixel in this reconstructed image corresponds to a predetermined area in physical space, and hence by multiplying the number of the turbulent pixels (white pixels) by this area, the real size of the patch can be calculated.

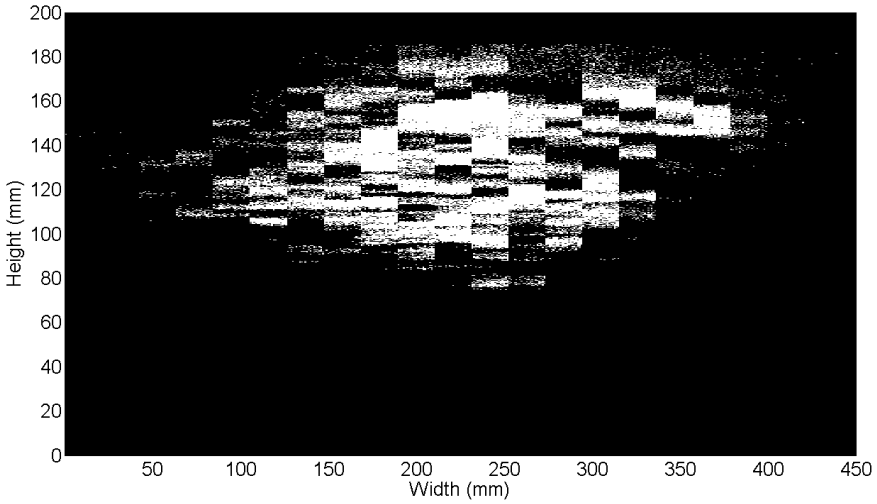

Figure C.2: A turbulent patch is reconstructed at $Re = 4810$. White areas indicate the image of the patch whereas black areas indicate the laminar flow.